

Time-Dependent Tomographic Reconstruction of the Solar Corona

D.Vibert^{a,*}, C.Peillon^a, P. Lamy^a, R.A. Frazin^b, J. Wojak^a

^a*Aix Marseille Université, CNRS, LAM (Laboratoire d'Astrophysique de Marseille) UMR 7326, 13388, Marseille, France*

^b*Dept. of Atmospheric, Oceanic and Space Sciences, University of Michigan, Ann Arbor, MI 48109, USA*

Abstract

Solar rotational tomography (SRT) applied to white-light coronal images observed at multiple aspect angles has been the preferred approach for determining the three-dimensional (3D) electron density structure of the solar corona. However, it is seriously hampered by the restrictive assumption that the corona is time-invariant which introduces significant errors in the reconstruction. We first explore several methods to mitigate the temporal variation of the corona by decoupling the “fast-varying” inner corona from the “slow-moving” outer corona using multiple masking (either by juxtaposition or recursive combination) and radial weighting. Weighting with a radial exponential profile provides some improvement over a classical reconstruction but only beyond $\approx 3 R_{\odot}$. We next consider a full time-dependent tomographic reconstruction involving spatio-temporal regularization and further introduce a co-rotating regularization aimed at preventing concentration of reconstructed density in the plane of the sky. Crucial to testing our procedure and properly tuning the regularization parameters is the introduction of a time-dependent MHD model of the corona based on observed magnetograms to build a time-series of synthetic images of the corona. Our procedure, which successfully reproduces the time-varying model corona, is finally applied to a set of 53 LASCO-C2 pB images roughly evenly spaced in time from 15 to 29 March 2009. Our procedure paves the way to a time-dependent tomographic reconstruction of the coronal electron density to the whole set of LASCO-C2 images presently spanning 20 years.

Keywords: Sun: Corona, Sun: Coronal Structures, Tomography

1. Introduction

Progress in understanding the physics of the corona and the solar wind depends upon empirical constraints on the three-dimensional (3D) distributions of the plasma properties such as temperature, density and magnetic field in the Sun's corona. Solar rotational tomography (SRT) uses coronal images observed at multiple aspect angles thanks to solar rotation to provide 3D reconstructions of the corona assuming that it does not vary in time, at least during the time interval necessary to achieve a complete view (typically half a solar rotation). When the images are at soft X-ray or EUV wavelengths, one can reconstruct both the temperature and the density in 3D from about $1.03 R_{\odot}$ to $1.25 R_{\odot}$ (the lower bound is greater than $1.0 R_{\odot}$ due to optical depth effects encountered in some spectral lines), via a process called differential emission measure tomography (DEMT), see Frazin et al. (2009) and Barbey et al. (2013). When the input images are coronagraphic white-light images of the K-corona, one may reconstruct the density at greater heights. For example, when the image data are from the LASCO-C2 coronagraph, the reconstruction region is roughly from $2.4 R_{\odot}$

to $5.5 R_{\odot}$ (Frazin and Janzen, 2002) and when the source is STEREO/COR1 the reconstruction region is between about $1.5 R_{\odot}$ to $4.0 R_{\odot}$ (Kramar et al., 2009; Kramar et al., 2014). In addition, the use of white-light coronagraph data has the potential of taking advantage of both the polarized brightness (pB) and total brightness (B) as independent sources of information (Frazin et al., 2010).

Whereas the determination of the 3D distribution of the coronal density (as well as temperature) is a highly desirable objective, SRT has fundamental limitations that have prevented it from becoming broadly accepted as a useful tool for solar science. Calibration uncertainty in the image data is important (Frazin et al., 2012), the finite field-of-view of the imaging instrument causes “pile-up” artifacts near the upper boundary (Frazin and Janzen, 2002; Frazin et al., 2010), and the $\approx 7^{\circ}$ tilt of the Sun's rotational pole relative to the ecliptic is theoretically a source of non-uniqueness, but the dominant source of error and uncertainty is the inherently dynamic nature of the solar corona so that it evolves as the Sun rotates. Thus, when one sees a movie of the corona, it is difficult to disentangle effects of the coronal dynamics from those of solar rotation, leading to a fundamental ambiguity and very serious artifacts in tomographic reconstructions of the corona as first shown by Frazin and Kamalabadi (2005).

Since then, a new method to perform time-dependent tomography involving Kalman filters was developed by

*Corresponding author

Email addresses: didier.vibert@lam.fr (D.Vibert), christelle.peillon@lam.fr (C.Peillon), philippe.lamy@lam.fr (P. Lamy), rfrazin@umich.edu (R.A. Frazin), julien.wojak@lam.fr (J. Wojak)

Butala et al. (2010) and applied to STEREO/COR1 images. It did improve the quality of the reconstruction by reducing the number of artifacts; however, and as we shall discuss later on, it faced several difficulties leaving the time-dependent tomography problem under-determined and the solution very reliant on the regularization choices. Moreover the complexity of the Kalman filter turns out to be of marginal utility due to the fact that we only have uninformative dynamical models of the corona at our disposal, whereas a time-dependent tomography can be achieved by a simpler multiple regularization approach as proposed in this article. Interestingly, the EUV tomography problem appears to be less compromised by this issue, most likely due to the fact that lines-of-sight that hit the solar disk (as well as those above the limb, as in the case of coronagraph data) are included in the inversion, which tend to stabilize the solution. Thus, to date, most scientific results from SRT have been produced with EUV tomography (Vázquez et al., 2009, 2010, 2011; Huang et al., 2012; Nuevo et al., 2013).

This article introduces several new strategies intended to mitigate the undesirable effects of coronal dynamics on tomographic reconstructions based on white-light coronagraph images. These new methods involve two different approaches:

1. For the part of the reconstruction located at a given radius r_0 and above, the goal is to de-emphasize the influence of coronal dynamics taking place at inferior radii ($r < r_0$). The rationale behind this is that, at large heights, the corona is less dense and tends to be less dynamic. Thus, it is hoped that the reconstruction at $r > r_0$ will not be “contaminated” by the contribution of material with line-of-sight at $r < r_0$. These procedures involve weighting and masking schemes. Part of the justification for this approach is that, strictly speaking, one does not need projections inferior to r_0 to reconstruct the part of the object at r_0 and above (Frazin et al., 2010; Louis and Natterer, 1983).
2. In using Kalman filters or spatio-temporal regularization for tomography of the solar corona, it has been observed that, unless very strong temporal regularization is used (greatly reducing the temporal variability of the solution), the reconstructed density tends to be concentrated in the plane that contains the Sun’s center and is perpendicular to the line-of-sight of the observation that was made at time t . Thus, the solution tracks the observation angle as the Sun rotates. The new strategy introduced to mitigate this effect is a novel type of spatio-temporal regularization, not based on gradients (as are most regularization operators), but instead specifically designed to suppress this rotational mode in the solution.

The lessons learned from these new strategies are likely applicable to tomography based on EUV images, but that

is not explored here.

The article is organized as follows: first, a general explanation of the tomographic reconstruction of the solar corona is given in Section 1. Then improved static reconstructions are described in Section 3. Next, time-dependent tomographic reconstruction methods are described in Section 4 and applied to model and real images. Finally, we conclude in Section 5.

2. Tomographic Reconstruction of the Solar Corona: General Considerations

2.1. Formulation of SRT as a Linear Problem

We present below the formulation of solar rotational tomography appropriate to the case of white-light images obtained with coronagraphs. Figure 1 illustrates the geometry for the Thomson scattering by a small volume of electrons located at a distance r from the Sun and the integration along the line-of-sight (denoted LOS thereafter) defined by its distance of closest approach (p) or impact parameter that produces the coronal radiance in a given pixel of the image. The small volume under consideration is at distance l from the point of closest approach of the LOS and it is convenient to define a scattering angle $\sin \theta = p/r$.

Following van de Hulst (1950), we can relate the local electron density (N_e) to the radiance measured in the j^{th} pixel of a coronal image via the integral along the LOS

$$y_j = \int_{-\infty}^{\infty} w[r(l_j), \theta(l_j)] N_e[r(l_j)] dl_j, \quad (1)$$

where the Thomson scattering function (w) depends upon the type of images, either unpolarized radiance “ B ” or polarized radiance “ pB ”, whose intensities are denoted as w_B and w_{pB} , respectively. Although the work here uses the more general expressions that include the finite size of the solar disk and limb darkening (van de Hulst, 1950), for simplicity we reproduce the approximate expressions given by Frazin et al. (2010), which are valid for a point-source of luminosity $4\pi L$:

$$w_B = \frac{3\sigma_e L}{8 p^2} [\sin^2 \theta(l_j) - \frac{1}{2} \sin^4 \theta(l_j)], \quad (2)$$

$$w_{pB} = \frac{3\sigma_e L}{16 p^2} \sin^4 \theta(l_j), \quad (3)$$

where σ_e is the Thomson cross section.

In order to reconstruct the corona, we need to observe it during at least one half of a solar rotation, that is 14 days, with a minimum cadence of about one image per day, but a higher cadence is highly desirable. Time intervals larger than one-half of a rotation are problematic for static reconstruction methods, creating many artifacts, because coronal dynamics causes inconsistency in the data. Then, for each pixel of each image, we have an equation along the corresponding LOS of the form of Equation (1).

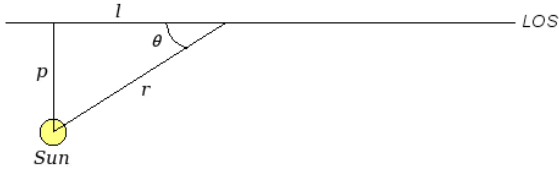


Figure 1: The geometry for the light scattering in the solar corona

The resulting system of equations is solved by adopting a discrete representation of N_e on a spherical grid (Frazin et al., 2009). Replacing the integrals by summations over discrete intervals, we now have to solve a system of linear equations:

$$\mathbf{y} = \mathbf{A}\mathbf{x} + \mathbf{n}, \quad (4)$$

where \mathbf{x} is a vector describing the discrete representation of N_e , \mathbf{y} is a vector containing the radiance values in all the pixels of the images, \mathbf{A} is a matrix calculated with Equation (2) or Equation (3), and \mathbf{n} is a Gaussian additive noise.

Let \mathbf{N} be the covariance matrix of this noise on the observed pixels. The maximum likelihood solution to Equation (4) is the least-squares solution:

$$\hat{\mathbf{x}} = \underset{\mathbf{x}}{\operatorname{argmin}} (\mathbf{y} - \mathbf{A}\mathbf{x})^\top \mathbf{N}^{-1} (\mathbf{y} - \mathbf{A}\mathbf{x}). \quad (5)$$

Assuming an independent and identically distributed (IID) Gaussian noise, the matrix \mathbf{N} is diagonal, isotropic and assumes the form $\mathbf{N} = \sigma^2 \mathbf{I}$. Then Equation (5) becomes:

$$\hat{\mathbf{x}} = \underset{\mathbf{x}}{\operatorname{argmin}} \|\mathbf{y} - \mathbf{A}\mathbf{x}\|_2^2. \quad (6)$$

If \mathbf{A} is not rank-deficient (more unknowns than independent equations), the analytic solution to Equation (5) is given by:

$$\hat{\mathbf{x}} = [\mathbf{A}^\top \mathbf{N}^{-1} \mathbf{A}]^{-1} \mathbf{A}^\top \mathbf{N}^{-1} \mathbf{y} \quad (7)$$

which, in the case of IID noise, simplifies to the solution of Equation (6):

$$\hat{\mathbf{x}} = [\mathbf{A}^\top \mathbf{A}]^{-1} \mathbf{A}^\top \mathbf{y}. \quad (8)$$

If \mathbf{A} is rank-deficient, then it has a non-empty null space and the solution to Equation (5) or (6) is not unique. But the inversion in Equation (7) or (8) can still be performed in the orthogonal complement of this null space. For most purposes, this amounts to choosing the solution of minimum norm, *i.e.* the one with no component in the null space of \mathbf{A} .

Although \mathbf{A} is sparse, its size makes explicit inversion of $[\mathbf{A}^\top \mathbf{A}]$ intractable but solutions can be computed via an iterative scheme, like the Lanczos bi-diagonalization named “LSQR” (Paige and Saunders, 1982), which converges to the minimum norm solution when \mathbf{A} is singular.

It is well known that SRT is an ill-posed or under-constrained problem resulting from the limited information available and further complicated by specific problems associated with coronal images obtained with externally-occulted coronagraphs.

1. The occulter blocks the solar disk and partially the inner corona (depending upon the exact design of the coronagraph); hence, the images contain information only beyond some minimum projected radius, for instance $\approx 2.2 R_\odot$ in the case of LASCO-C2, resulting in so-called hollow projections.
2. An additional difficulty comes from the outer limit r_{max} of the field-of-view of the instrument whereas the LOS integrals include contributions from electrons located beyond this distance. It is necessary to include in the reconstruction all parts of the corona that contribute to the observed signal and that includes those beyond r_{max} , see the discussion in Frazin et al. (2010).
3. The image cadence is usually limited to a few images per day while the Sun and its corona rotates at about 13° per day, thus resulting in limited angular sampling.
4. A final minor point concerns the view of the corona restricted to the ecliptic plane implying that each of the line integral paths is parallel to this plane which is not perpendicular to the sun rotation axis.

These problems lead to a measurement matrix (\mathbf{A}) that is not only singular, but poorly conditioned (small singular values). The direct consequence is that the solution of Equation (7) or (8) is very noisy and not robust — a small change in the data has a large impact on the solution — because of the division by the very small singular values. To circumvent these limitations, we introduce a-priori knowledge of the solution, a process known as regularization.

2.2. Regularization of the SRT Problem

2.2.1. Tikhonov Regularization

We first introduce the Tikhonov regularization which adds a penalty term to the likelihood function enforcing a-priori properties of the solution, for instance smoothness. This translates to solving the following equation:

$$\hat{\mathbf{x}} = \underset{\mathbf{x}}{\operatorname{argmin}} \|\mathbf{y} - \mathbf{A}\mathbf{x}\|_2^2 + \lambda^2 \|\mathbf{S}\mathbf{x}\|_2^2, \quad (9)$$

where $\|\mathbf{S}\mathbf{x}\|_2^2$ is the regularization term, λ the regularization parameter, and \mathbf{S} the regularization operator. The choice of the proper regularization has been thoroughly discussed by Frazin et al. (2007) and we follow their recommendations of using the second derivatives with respect to the angular spherical coordinates (θ, ϕ) — except that we add the distance r in order to remove radial noise — and a single regularization parameter.

Equation (9) can now be rewritten

$$\hat{\mathbf{x}} = \underset{\mathbf{x}}{\operatorname{argmin}} \left\| \begin{pmatrix} \mathbf{y} \\ \mathbf{0} \end{pmatrix} - \begin{pmatrix} \mathbf{A} \\ \lambda \mathbf{S} \end{pmatrix} \mathbf{x} \right\|_2^2, \quad (10)$$

whose analytic solution is

$$\hat{\mathbf{x}} = (\mathbf{A}^\top \mathbf{A} + \lambda^2 \mathbf{S}^\top \mathbf{S})^{-1} \mathbf{A}^\top \mathbf{y}, \quad (11)$$

which can be solved in the same manner as the unregularized linear least-square problem.

Having settled the regularization procedure, it remains to properly tune the regularization parameter (λ) controlling the balance between the fidelity of the solution to the data and the level of regularization. The strategy in the specific case of coronagraphic SRT has been extensively discussed by Frazin (2000) and Frazin and Janzen (2002). Barbey et al. (2013) later argued that this parameter can be determined in an unsupervised way, using a Bayesian formalism and adopting a probability distribution law for it. This however leads to prohibitively time-consuming algorithms, as pointed out, for instance, by Orioux et al. (2013). Turning therefore to the supervised method, classical approaches are the L-curve (Hansen, 1992; Hansen and OLeary, 1993), cross-validation (Stone, 1974; Allen, 1974; Frazin and Janzen, 2002 and references therein), and the generalized cross-validation (Golub et al., 1979) known as “GCV”.

The cross-validation requires performing several inversions and, at each time, on a different training set built by removing some of the observed pixels and then predicting the removed ones. This is repeated for several values of λ and finally, the value leading to the best prediction is selected. This procedure is very resource-consuming and we thus focus on the two other.

The principle of the L-curve is to determine the best compromise by looking at the shape of the curve displaying the residual error ($\|\mathbf{y} - \mathbf{A}\hat{\mathbf{x}}(\lambda)\|$) versus the regularization semi-norm ($\|\mathbf{S}\hat{\mathbf{x}}(\lambda)\|$) for each λ . The optimum point of this L-shaped curve is taken at its maximum curvature.

GCV was developed to find the same compromise as cross-validation by simply minimizing the following analytic expression:

$$\underset{\lambda}{\operatorname{argmin}} \frac{m \|\mathbf{I} - \mathbf{K}\|_2^2}{(\operatorname{trace}(\mathbf{I} - \mathbf{K}))^2}, \quad (12)$$

where the operator \mathbf{K} , often denoted “hat-matrix”, produces the estimated observation from the data such that $\mathbf{I} - \mathbf{K}$ is the operator computing the residual:

$$\mathbf{K} = \mathbf{A}(\mathbf{A}^\top \mathbf{A} + \lambda^2 \mathbf{S}^\top \mathbf{S})^{-1} \mathbf{A}^\top.$$

The difficulty with this expression lies in computing the denominator. This would in principle require performing several inversions as in the case of simple cross-validation. But following Golub and Von Matt (1997), we can use an approximation limiting the task to performing an inversion

on one random vector (\mathbf{u}) containing -1 or +1 elements with uniform probability. Then

$$\hat{\mathbf{t}}(\lambda) = \mathbf{u}^\top (\mathbf{I} - \mathbf{K}) \mathbf{u} \quad (13)$$

is an unbiased estimator of $\mathbf{t}(\lambda) = \operatorname{trace}(\mathbf{I} - \mathbf{K})$.

The regularization introduced in this section should be able to partly cope with the difficulties listed at the end of Section 2.1, particularly the low cadence of images. In the practical case of the LASCO-C2 images, Frazin et al. (2007) studied a two-week time period during which the instrument took about 85 *pB* images in order to ascertain the importance of the cadence for the quality of the reconstruction. Their principal finding is that, beyond a certain cadence, there is no benefit in taking more images, although higher cadences do not have negative consequences. This is due to the dynamical nature of the solar corona which imposes a fundamental limitation to the spatial resolution of the reconstruction.

2.2.2. Constraint on the Lower Bound

As the electron density is a strictly positive function, a positivity constraint can be applied. The algorithms usually chosen to solve non-negative linear least-square problems are “NNLS” (Lawson and Hanson, 1995) and its modified versions such as “fast-NNLS” (Bro and De Jong, 1997) or the more general “BVLS” (Stark and Parker, 1995) algorithm which handles arbitrary lower and upper bounds. However, the “L-BFGS-B” algorithm (Byrd et al., 1995) developed for the minimization of more general convex functions instead of specific linear least-square minimizations turns out to be much faster for the same level of accuracy in its latest version (Morales and Nocedal, 2011) and was therefore adopted here.

In practice, the above positivity constraint unfortunately tends to set negative values to zero and is therefore of limited interest as it will be shown later (Section 2.3.2). This difficulty may be circumvented by introducing an a-priori electron density minimal background and constraining the reconstructed solution to be larger. This is easy to achieve since the L-BFGS-B algorithm is actually able to deal with any box-constraint and we can set the lower bound of the solution to be the minimal background. However, we choose another path consisting in subtracting the observed minimal background (\mathbf{Ab}) from the data, then performing the inversion using the positivity constraint, and finally adding the background (\mathbf{b}) to the solution:

$$\hat{\mathbf{x}} = \mathbf{b} + \underset{\mathbf{s} \geq 0}{\operatorname{argmin}} \left(\|\mathbf{y} - \mathbf{Ab} - \mathbf{As}\|_2^2 + \lambda^2 \|\mathbf{Ss}\|_2^2 \right). \quad (14)$$

The advantage of this approach versus the direct minimum background lower bound constraint is that the regularization operator is applied to the structures of the corona without the background, since it has been subtracted.

2.3. Illustration of SRT Reconstruction of an MHD Model of the Corona

We now make use of the three-dimensional magneto-hydrodynamic (MHD) simulation of the solar corona presented in [Appendix A](#) to test the above SRT procedure. The MHD simulation is a steady-state model and we obtain temporal variability with a sequence of steady-state models, each with a different synoptic magnetogram specifying the lower boundary. The synthetic daily pB images calculated from the 3-D electron density resulting from the MHD simulation are ingested by the computer program and the solutions for the electron density are compared to the original input. We adopt boundary radial distances on the synthetic images of $r_0 = 2.5 R_\odot$ and $r_{max} = 6.2 R_\odot$ consistent with the LASCO-C2 images to be analyzed later on. We perform the reconstruction on an enlarged spherical grid of $8.5 R_\odot$ to include LOS contributions beyond r_{max} as pointed out in [Section 2.1](#). The grid has constant resolutions of $0.1 R_\odot$ in the radial direction and of 3° in both longitude and latitude.

2.3.1. Static Reconstruction of a Static Model Corona

As a first exercise, we process synthetic images obtained from 14 viewpoints (one per day) as seen from the SOHO orbit using a single steady-state MHD model, that is considering a static corona. The third row of [Figure 2](#) displays the result for which the regularization parameter (λ) is determined using the “GCV” method.

The excellent agreement with the original MHD electron density distribution proves that the regularization is working very well and is indeed able to cope with the limitations of the coronagraph images as listed at the end of [Section 2.1](#).

In order to further check that the determination of the regularization parameter is optimal, we perform the reconstruction with different values of the regularization parameter (λ). Two examples are shown in [Figure 2](#): when λ is larger than the nominal value, the solution is too smooth whereas high frequency noise appears when it is smaller. Also note the zero density artifacts (hereafter ZDA) that arise when λ is too large. We finally compute the normalized RMS error between the reconstruction and original electron distribution which we classically define at each radial distance from the Sun as the root mean squared error normalized by the standard deviation of the model:

$$\mathcal{E}_{\text{rms}}(r) = \frac{1}{\sigma(r)} \sqrt{\frac{1}{N} \sum_{\theta, \phi} (\hat{x}_{r, \theta, \phi} - x_{r, \theta, \phi})^2}, \quad (15)$$

where

$$\sigma(r)^2 = \frac{1}{N} \sum_{\theta, \phi} (x_{r, \theta, \phi} - \bar{x}(r))^2$$

and

$$\bar{x}(r) = \frac{1}{N} \sum_{\theta, \phi} x_{r, \theta, \phi}.$$

We verify that the chosen optimal value for λ is that which minimizes this normalized RMS error.

2.3.2. Static Reconstruction of a Dynamic Model

We now consider the more realistic case of a dynamic corona. For each of the above 14 viewpoints, we input the synthetic images from the dynamic MHD model generated at the actual times LASCO took pB sequences (November 2008). Thus, the observation geometry was identical to the case of static reconstruction of a static model corona in [Section 2.3.1](#). [Figure 3](#) compares the two reconstructions for a static and a dynamic corona. In the latter case, the static reconstruction is unable to cope even with small temporal variations typical of a minimum of solar activity: the ZDAs are overwhelming and render the solution useless. The problem most likely stems from the slow motion of sharp coronal structures (prominently the streamer belt), as static reconstruction methods cannot distinguish between the effects of rotation and dynamics.

2.4. Additional Difficulties Associated with SRT

In addition to the difficulties associated with the facts that the SRT is an ill-posed problem and that the corona varies with time, we briefly summarize below additional difficulties that SRT faces.

1. Coronal images are affected by various instrumental problems which are difficult to calibrate and correct, for instance imperfect removal of instrumental stray light and uncertainties in the polarization measurements.
2. In addition, in the case of the coronal radiance B , assumptions are required to perform the separation of the K and F components which may therefore be imperfect.
3. The corona is further perturbed by coronal mass ejections (CMEs); affected frames may be removed or masked to alleviate the problem ([Frazin, 2000](#)) but this does not eliminate the abrupt reconfigurations of the global coronal structure that sometime take place following the eruption of a CME ([Floyd et al., 2014](#)).

Several of the above difficulties are inherent to the corona and its techniques of observations and thus cannot be circumvented.

3. Static Reconstructions Mitigating Artifacts Due to Temporal Variations

As temporal variations are strongest in the inner corona and tend to decrease with distance, we suspect that the current SRT reconstruction algorithms unduly propagate outward artifacts created by the highly dynamic inner corona, due to the coupled nature of the linear system of equations. We suggest two different procedures to mitigate this effect, both at the expense of losing optimality in the statistic sense of [Equation \(9\)](#): i) masking the inner corona when reconstructing the outer part and ii) radially weighting the electron density to counterbalance its steep gradient.

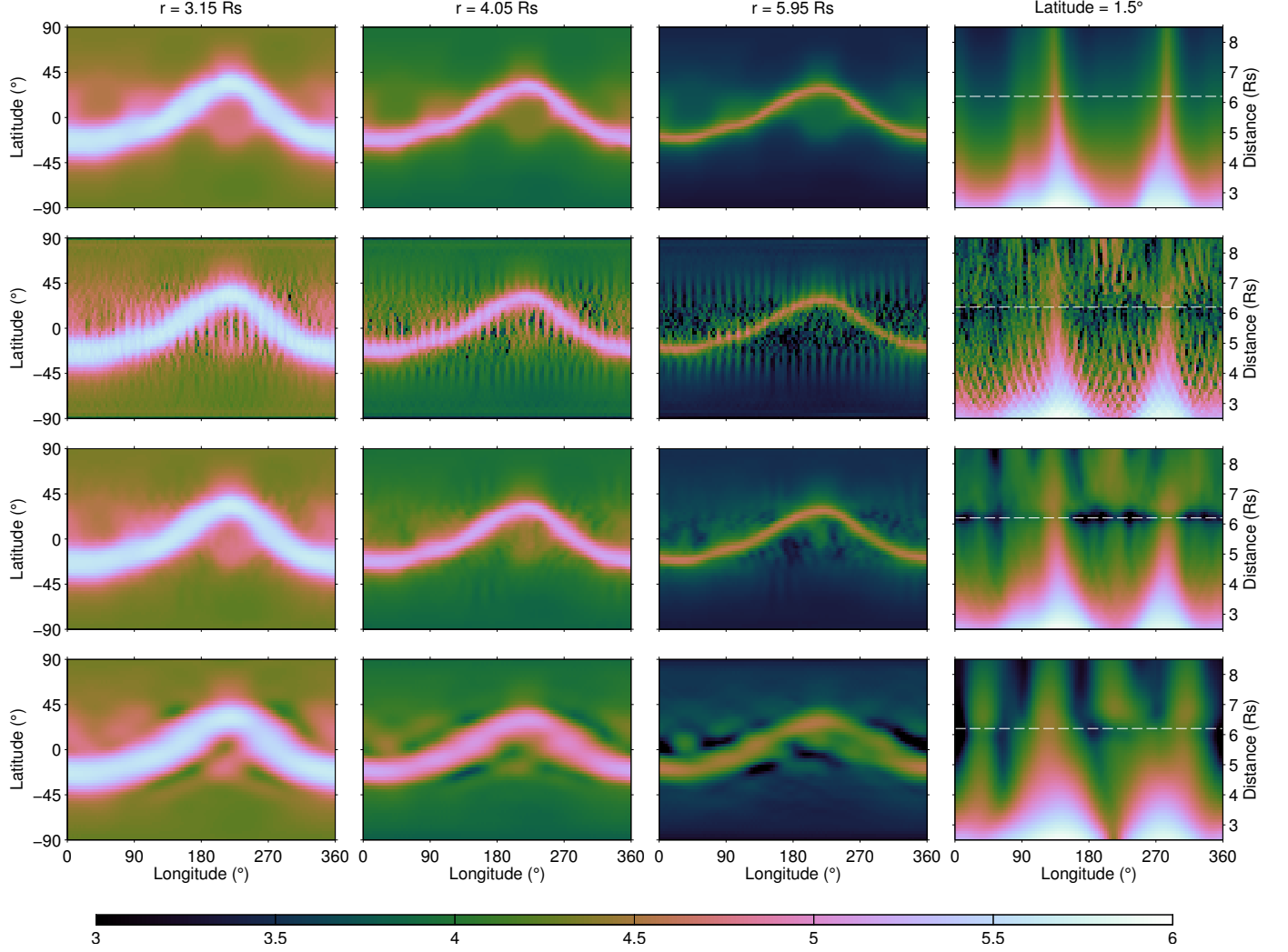
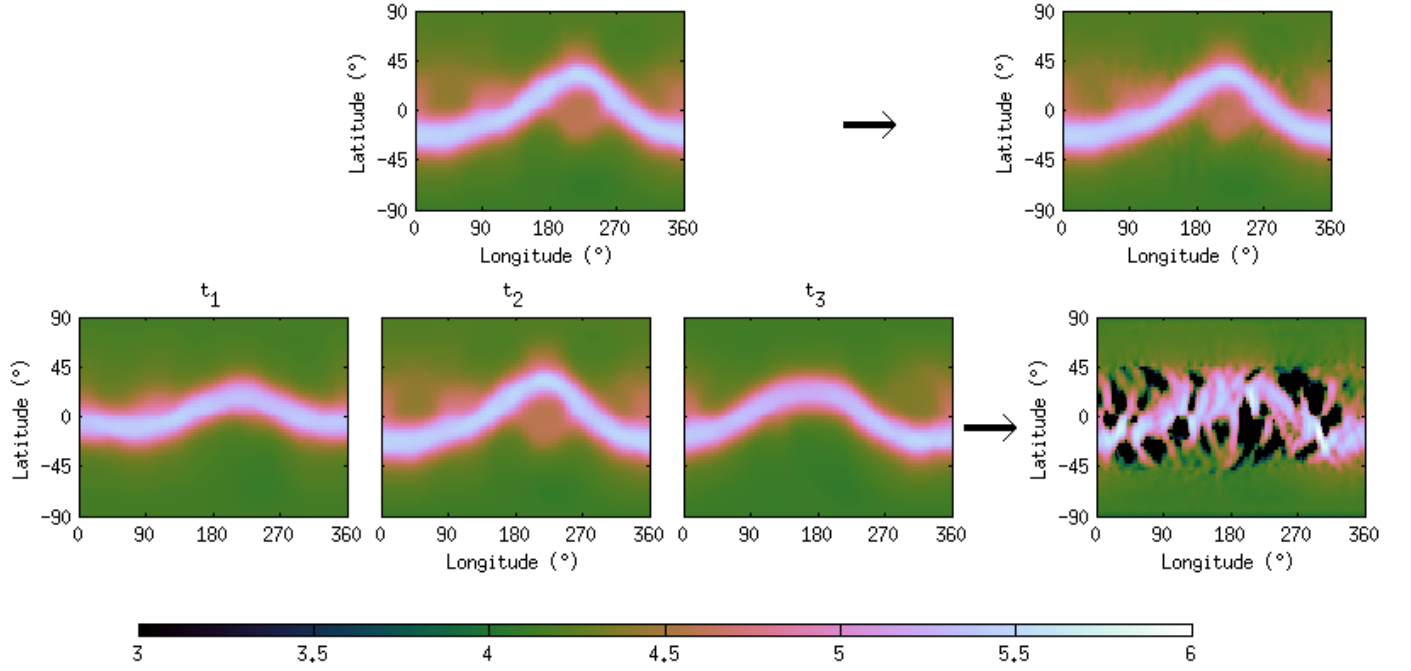


Figure 2: Illustration of spatially regularized static reconstructions of a static model for 3 different choices of the regularization parameter. The 16 panels represent slices of the electron density in units of cm^{-3} using a logarithmic scale. The 3 leftmost columns correspond to spherical shells centered at radii of $3.15 R_{\odot}$, $4.05 R_{\odot}$ and $5.95 R_{\odot}$ and the rightmost column corresponds to the equatorial plane (seen in polar coordinates). The first (top) row corresponds to the model and the next 3 rows to reconstructions with different values of the regularization parameter (λ): 1×10^{-7} (second row), the optimal value 1×10^{-6} (third row), and 2×10^{-5} (fourth, bottom row). The white dashed line in the four panels of the rightmost column corresponds to the practical limit of the useful field-of-view ($6.2 R_{\odot}$).

(a)



(b)

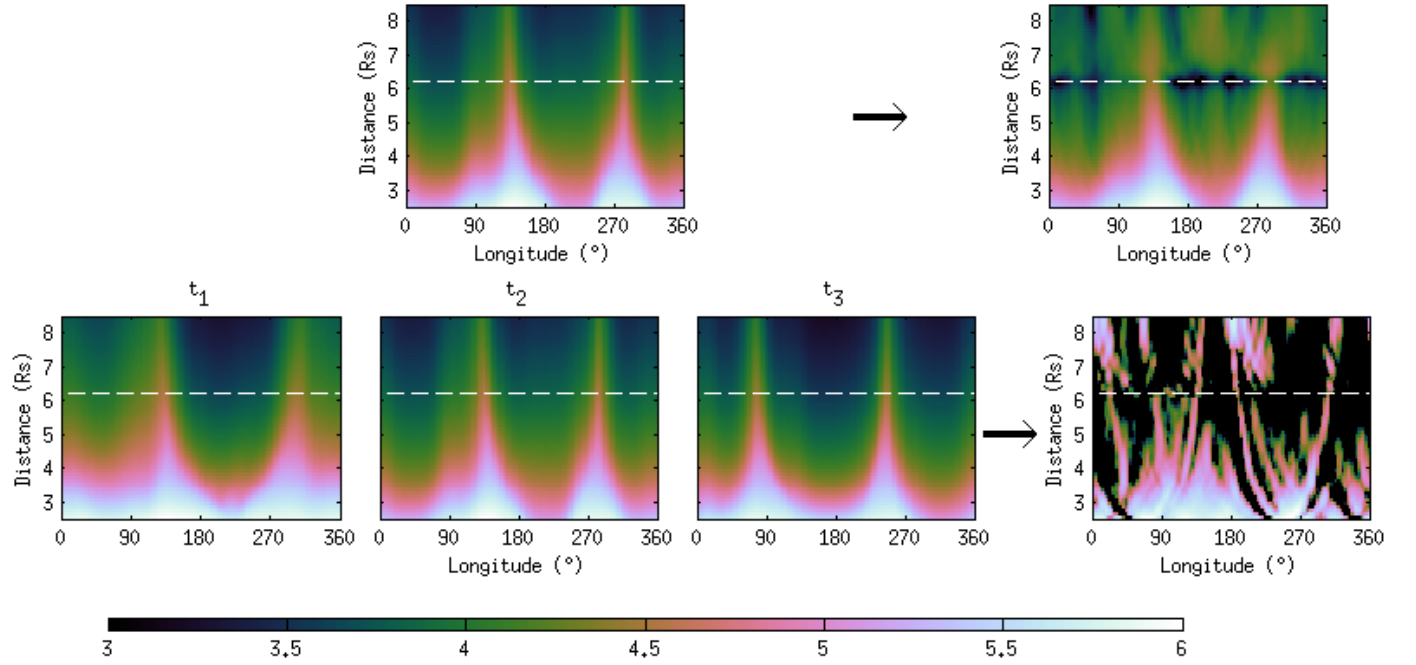


Figure 3: (a) Comparison of the standard static reconstruction with spatial regularization applied to two cases of a model corona, a static one (top row) and a dynamic one (bottom row). Each image represents a slice at constant radius ($r = 3.45 R_\odot$) of the electron density in units of cm^{-3} using a logarithmic scale. The images on the left correspond to the model, and the rightmost image corresponds to the reconstruction. The time interval between each image of the dynamic model is 6 days. (b) Same as (a) with the images showing the equatorial plane in polar coordinates.

3.1. Reconstruction with Multiple Masking

The simple scheme of using two or more masks and juxtaposing the resulting solutions unsurprisingly creates radial discontinuities. To enforce radial continuity, we introduce multiple masking in a recursive way, starting from the mask of largest radius, and using the solution obtained at step (n) in the reconstruction at step $(n+1)$.

Let $\{r^{(n)}, n \in [1, \dots, N]\}$ be the set of decreasing radii of the masks at each step (n) and let $\hat{\mathbf{x}}^{(n-1)}$ be the estimated solution at step $(n-1)$ valid from $r^{(n-1)}$ to r_{\max} . At iteration (n) , we subtract from the masked data ($\mathbf{y}^{(n)}$) the projected image corresponding to $\hat{\mathbf{x}}^{(n-1)}$ and solve for the remaining shell of the corona ($\Delta\mathbf{x}^{(n)}$) extending from $r^{(n)}$ to $r^{(n-1)}$ (Figure 4). To maintain radial continuity of the regularization operator through each step, we adopt the same scheme and solve the following equation at step (n) :

$$\begin{aligned} \Delta\hat{\mathbf{x}}^{(n)} = \operatorname{argmin}_{\Delta\mathbf{x} \geq 0} & \left(\left\| \mathbf{y}^{(n)} - \mathbf{C}^{(n)}\hat{\mathbf{x}}^{(n-1)} - \mathbf{B}^{(n)}\Delta\mathbf{x} \right\|_2^2 \right. \\ & \left. + \lambda^2 \left\| -\mathbf{S}^{(n-1)}\hat{\mathbf{x}}^{(n-1)} - \Delta\mathbf{S}^{(n)}\Delta\mathbf{x} \right\|_2^2 \right), \end{aligned} \quad (16)$$

where $\mathbf{C}^{(n)}$ are the columns going from $r^{(n-1)}$ to r_{\max} of the “masked” matrix ($\mathbf{A}^{(n)}$) which is the matrix \mathbf{A} without the lines corresponding to masked pixels below $r^{(n)}$. $\mathbf{B}^{(n)}$ are the remaining columns going from $r^{(n)}$ to $r^{(n-1)}$, see Figure 4. $\mathbf{S}^{(n-1)}$ is built from the columns of \mathbf{S} going from $r^{(n-1)}$ to r_{\max} . The regularization matrix ($\Delta\mathbf{S}^{(n)}$) corresponding to the shell ($\Delta\mathbf{x}^{(n)}$) is built from the columns of \mathbf{S} going from $r^{(n)}$ to $r^{(n-1)}$.

Note that we could introduce a different value of λ at each step. We did test this possibility but did not see much change; therefore a unique regularization parameter (λ) has been used at all steps.

Finally, the estimated solution at iteration (n) is the juxtaposition of the previous solution ($\hat{\mathbf{x}}^{(n-1)}$) and the above shell ($\Delta\mathbf{x}^{(n)}$):

$$\hat{\mathbf{x}}^{(n)} = [\Delta\mathbf{x}^{(n)}; \hat{\mathbf{x}}^{(n-1)}], \quad (17)$$

where the semicolon indicates column stacking; thus, $\hat{\mathbf{x}}^{(n)}$ is a column vector consisting of the two smaller column vectors $\Delta\mathbf{x}^{(n)}$ and $\hat{\mathbf{x}}^{(n-1)}$.

3.2. Reconstruction with Radial Weighting

Introducing a radial weighting of the images in the least-square minimization requires defining a proper weighting function. In treating the temporal variations of the corona as noise in the observed images, we note that its variance decreases with increasing distance from the Sun. Therefore the coefficients of the diagonal covariance matrix (\mathbf{N}), which were originally set to the constant σ^2 , can be replaced by a radial function ($f(\mathbf{r})$) which expresses an appropriate weighting. Writing $\mathbf{N} = \operatorname{diag}(f(\mathbf{r}))$ and introducing $\mathbf{A}' = \operatorname{diag}(\sqrt{f(\mathbf{r})})\mathbf{A}$ and $\mathbf{y}' = \operatorname{diag}(\sqrt{f(\mathbf{r})})\mathbf{y}$,

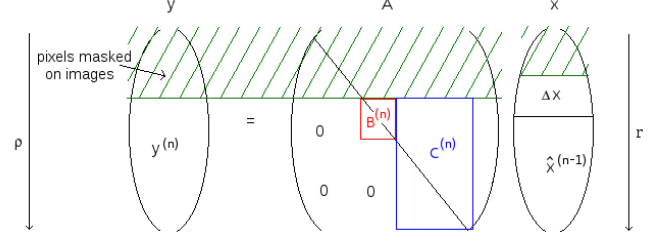


Figure 4: Illustration of the sub-matrices used in the multiple masking procedure with successive combination of solutions.

the equation to be solved is identical to the original Equation (8) after substituting \mathbf{A} by \mathbf{A}' and \mathbf{y} by \mathbf{y}' .

We tested two functions $f(\mathbf{r})$: the mean radial profile of the coronal radiance and an exponential function defined by:

$$f(r) = \begin{cases} e^{\frac{b-r}{c}} & \text{for } r \leq b \\ 1 & \text{for } r > b \end{cases} \quad (18)$$

where b is the radius beyond which the weighting is no longer necessary and c controls the sharpness of the weighting for $r_{\min} < r < b$.

3.3. Illustration and Comparison of the Methods of Reconstruction

We first test the above procedures using the MHD model presented in Appendix A. The results are illustrated and compared in Figure 5 which displays images of the electron density and in Figure 6 which quantifies the errors associated with each procedure in spherical shells of increasing distance from the Sun: i) the percentage of ZDAs in the solution (which would have corresponded to negative values in the general case without the positivity constraint) and ii) the RMS error normalized by the standard deviation (see Equation (15)).

Multiple masking, either by juxtaposition or recursive combination, offers an improvement of the reconstruction limited to the outer corona ($> 4 R_{\odot}$) as expected since it avoids propagating dynamic changes to this region. Simple juxtaposition naturally introduces radial discontinuities which are alleviated by recursive combination at the price of a degraded reconstruction in the inner part ($\leq 4 R_{\odot}$) to the point of being worse than the standard, unmasked reconstruction. This is because of the accumulation of errors from the outer corona to the inner corona during the recursive process.

Radial weighting leads to the opposite trend as the reconstruction is improved in the inner corona but degraded in the outer part, but still superior to the standard one. Weighting with an exponential profile globally leads to a better reconstruction than weighting with the radiance profile of the corona except inside $\approx 3 R_{\odot}$ where the solution is over-smoothed; indeed it introduces too much weighting as the regularization term dominates in the minimization.

Inside $3 R_{\odot}$, none of the proposed methods improves the reconstruction. From $3 R_{\odot}$ to $5 R_{\odot}$, the weighting method with an exponential profile gives the best result whereas beyond $5 R_{\odot}$, this is achieved by multiple masking with juxtaposition. In summary, these methods allow improving the quality of the reconstruction in the regimes where they perform best, decreasing the percentage of ZDA and the RMS error by a factor ≈ 2 compared to the standard method but still much inferior to the performance of the reconstruction of a static corona.

An interesting remark concerns the number of ZDA which is generally a good proxy for the RMS error. Therefore, it offers a relevant quality factor for the reconstruction of real data for which the error is obviously not available.

We extend the comparison to the set of 53 LASCO-C2 *pB* images as described in Appendix B and display the results in Figure 7. Since we do not have a model, we cannot compute the error of the reconstruction; instead, we compute the residual errors between the observed and the synthetic images calculated from the reconstructed N_e (Figure 8). The pros and cons of the different procedures are consistent with those reached in the case of the MHD model. Incidentally, the percentages of ZDA are similar which suggests that the MHD model is adequate to perform the validity tests.

4. Time-Dependent Reconstruction

4.1. General Formalism

As we have seen, time-dependency of the corona is the fundamental difficulty for SRT. Strategies for mitigating the problem were first discussed in Frazin et al. (2005). A Kalman filter solution was finally implemented by Butala et al. (2010), but the performance was not greatly superior to static reconstruction, due to the highly under-determined nature of attempting to infer the evolving state of the corona given only one or a few simultaneous viewpoints.

4.1.1. Spatio-temporal Regularization

Several spatio-temporal regularization methods exist to solve the problem (Zhang et al., 2005). We focus our attention to:

- the state-space model using Kalman smoother implemented by Butala et al. (2010);
- the multiple constraint regularization mentioned by Barbey et al. (2008) and Barbey et al. (2013).

The theoretical solutions of both methods are identical for some specific choices of the operators and covariance matrices: i) scalar multiple identity matrices for both the Kalman state transition matrix and the time covariance matrix in the case of the “Kalman” approach and ii) an upper or lower bi-diagonal time-regularization operator for

the multiple constraint approach. In this work, we choose the multiple constraint method since it is simpler to implement and offers a direct interpretation of the smoothness constraints in space and time.

The vector (\mathbf{x}) to be reconstructed is now time-dependent. Let stack each static corona (\mathbf{x}_i) at each time (t_i) in one single vector: $\bar{\mathbf{x}} = \{\mathbf{x}_1; \mathbf{x}_2; \dots; \mathbf{x}_{N_t}\}$. The spatio-temporal linear measurement system becomes:

$$\bar{\mathbf{y}} = \bar{\mathbf{A}} \bar{\mathbf{x}}, \quad (19)$$

where $\bar{\mathbf{y}} = \mathbf{y} = \{\mathbf{y}_1; \mathbf{y}_2; \dots; \mathbf{y}_{N_t}\}$ are the stacked vectors of pixels radiance in each image. This vector represents the observed data. It has the same number of elements and is arranged in the same way as the \mathbf{y} vector of the static reconstruction. The dynamic measurement matrix $(\bar{\mathbf{A}})$ is composed of the blocks of the static matrix (\mathbf{A}) that correspond to the measurements at a given observation time. If

$$\mathbf{A} = \begin{pmatrix} \mathbf{A}_1 \\ \mathbf{A}_2 \\ \vdots \\ \mathbf{A}_{N_t} \end{pmatrix}, \text{ then } \bar{\mathbf{A}} = \begin{pmatrix} \mathbf{A}_1 & & & \\ & \mathbf{A}_2 & & \\ & & \ddots & \\ & & & \mathbf{A}_{N_t} \end{pmatrix}. \quad (20)$$

We then restrict our procedure to the simplest form of the multiple constraint regularization with one “pure” spatial and one “pure” temporal regularization where the spatial (resp. temporal) constraint is the same at each time instant (resp. voxel).

The solution is then:

$$\hat{\bar{\mathbf{x}}} = \underset{\bar{\mathbf{x}} \geq 0}{\operatorname{argmin}} \left\| \mathbf{y} - \bar{\mathbf{A}} \bar{\mathbf{x}} \right\|_2^2 + \lambda_s^2 \left\| \bar{\mathbf{S}} \bar{\mathbf{x}} \right\|_2^2 + \lambda_t^2 \left\| \bar{\mathbf{T}} \bar{\mathbf{x}} \right\|_2^2, \quad (21)$$

where $\bar{\mathbf{S}} = \mathbf{I}_{N_t} \otimes \mathbf{S}$ and $\bar{\mathbf{T}} = \mathbf{T} \otimes \mathbf{I}_{N_{\text{voxels}}}$ are the “pure” spatial and temporal regularizations, λ_s and λ_t being the spatial and temporal regularization parameters. The symbol \otimes represents the Kronecker product and \mathbf{I}_{N_t} (resp. $\mathbf{I}_{N_{\text{voxels}}}$), the identity matrix of dimension N_t , the number of time steps or images (resp. the identity matrix of dimension N_{voxel} , the number of voxels).

Note that $\bar{\mathbf{T}}$ applies to the same spatial measurements from all time instants and constrains its temporal behavior according to \mathbf{T} . Each row of \mathbf{T} acts as a temporal high-pass filter selectively passing undesirable components to be minimized in the reconstruction.

For the temporal regularization operator \mathbf{T} , we choose to implement the first derivative to enforce smoothness. This operator is bi-diagonal since it filters two consecutive states for each voxel. In this case, a Kalman smoothing with an identity state-transition matrix theoretically produces the same solution, but the convergence algorithm is different.

As in Equation (10), we can stack the observation and regularization matrices in one single matrix and rewrite Equation (21) as a simple, non-negative linear least-square

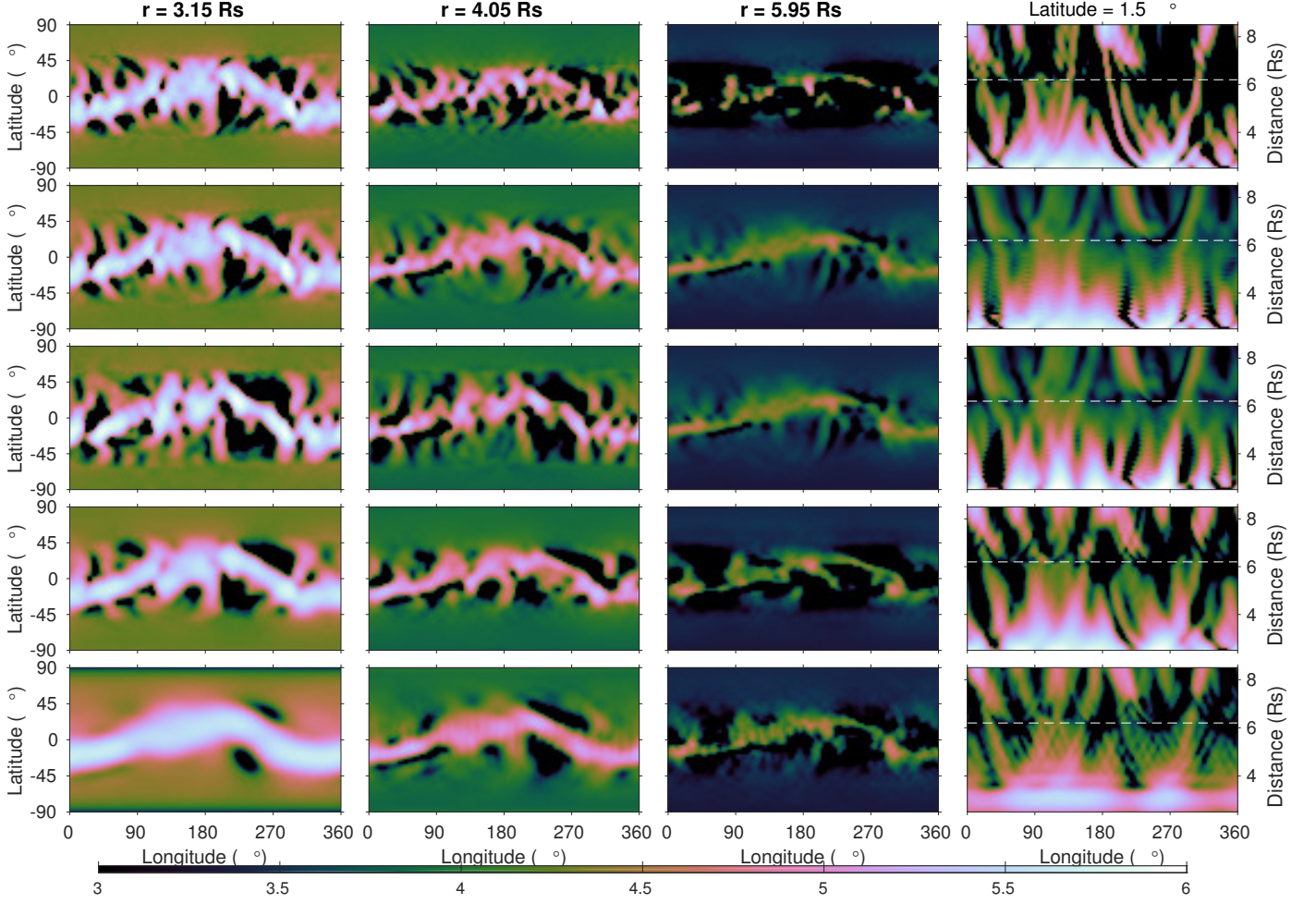


Figure 5: Comparison of five static reconstruction procedures applied to a dynamic (MHD) model of the corona as displayed in Figure A.18. The 20 panels represent slices of the electron density in units of cm^{-3} using a logarithmic scale. Each row corresponds to one of the static reconstruction methods: the standard spatial regularization (top row), multiple masking with simple juxtaposition (second row) and recursive combination of solutions (third row), radial weighting with a mean radial intensity profile (fourth row) and an exponential profile with $b = 5$ and $c = 0.25$ (bottom row). The 3 leftmost columns correspond to spherical shells at $3.15 R_{\odot}$, $4.05 R_{\odot}$ and $5.95 R_{\odot}$ and the rightmost column to the equatorial plane in polar coordinates.

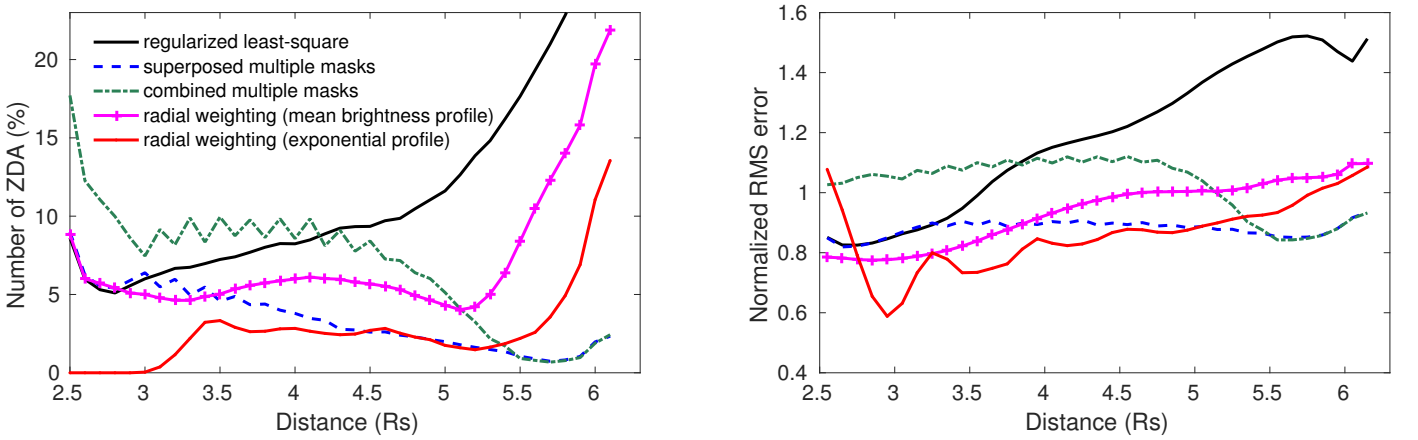


Figure 6: Illustrations of the errors associated with the five static reconstruction procedures applied to a dynamic model of the corona, in spherical shells of increasing distance from the Sun. The left panel presents the percentage of ZDA (Zero Density Artifacts). The right panel presents the RMS error normalized by the standard deviation of the model.

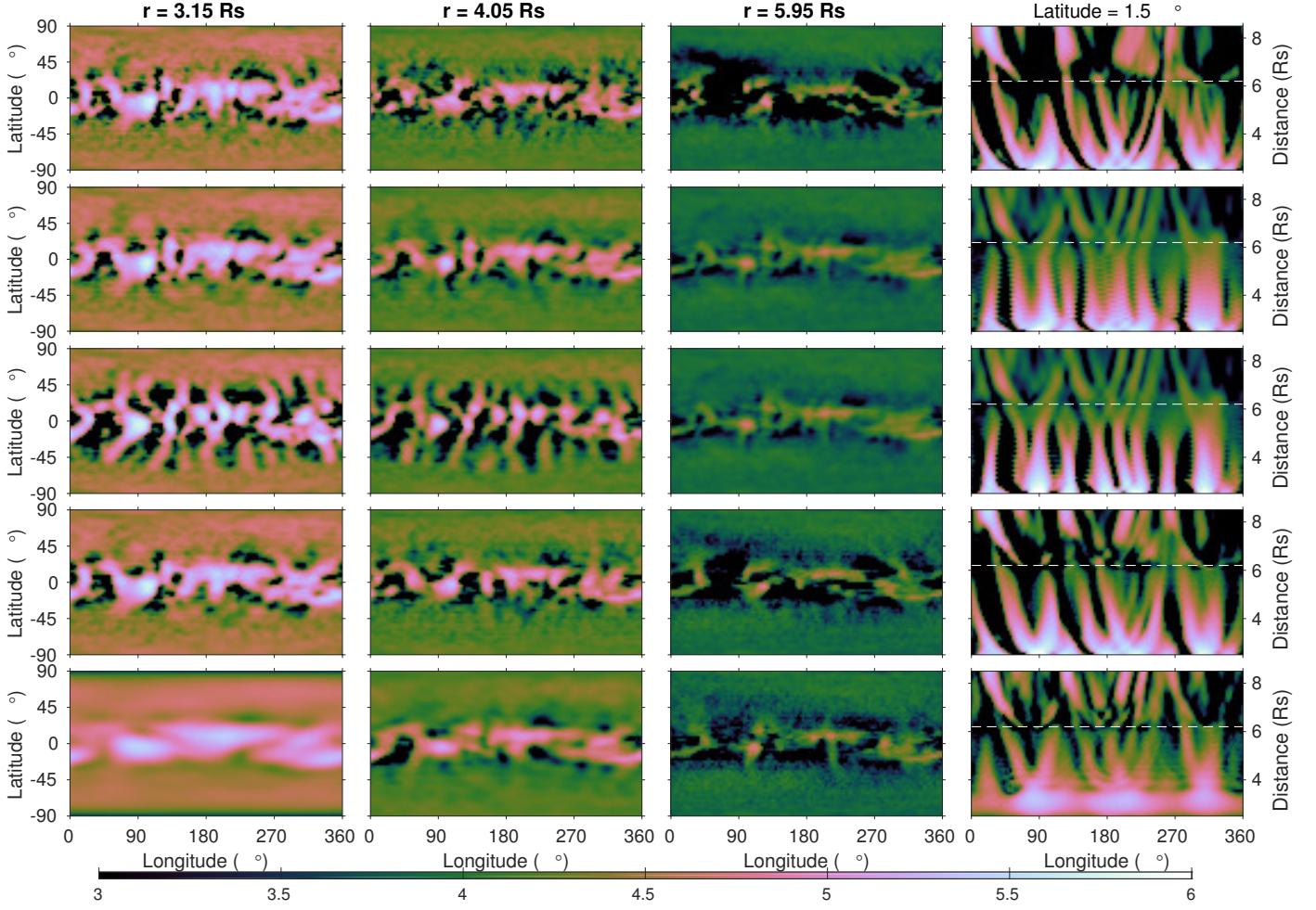


Figure 7: Comparison of the five static reconstruction procedures applied to 53 LASCO-C2 pB images. The 20 panels represent slices of the tomographic determinations of the electron density in units of cm^{-3} using a logarithmic scale. The 3 leftmost columns correspond to spherical shells with radii of $3.15 R_{\odot}$, $4.05 R_{\odot}$ and $5.95 R_{\odot}$ and the rightmost column to the equator. Each row corresponds to one of the static reconstruction methods: the standard spatial regularization (first row), multiple masking with simple juxtaposition (second row) and successive combination (third row) of solutions, radial weighting with a mean radial intensity profile (fourth row) and an exponential profile (fifth row).

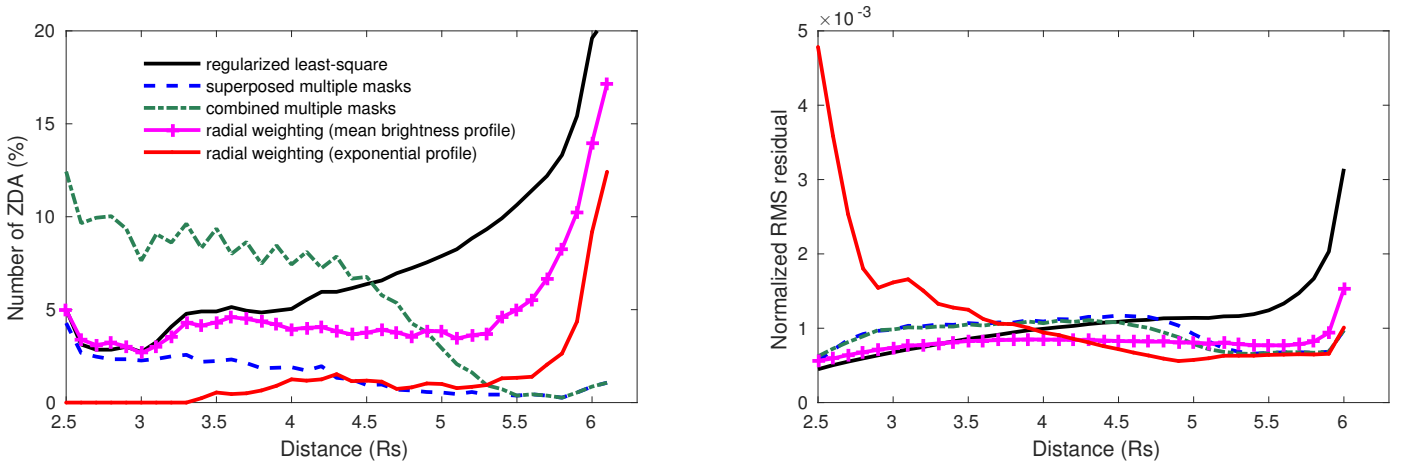


Figure 8: Illustrations of the errors associated with the five static reconstruction procedures applied to 53 LASCO-C2 pB images, in spherical shells of increasing distance from the Sun. The left panel presents the percentage of ZDA. The right panel presents the RMS residual error normalized by the standard deviation of the image pixels.

minimization which can be solved using the L-BFGS-B algorithm:

$$\hat{\mathbf{x}} = \underset{\bar{\mathbf{x}} \geq 0}{\operatorname{argmin}} \left\| \begin{pmatrix} \mathbf{y} \\ \mathbf{0} \\ \mathbf{0} \end{pmatrix} - \begin{pmatrix} \bar{\mathbf{A}} \\ \lambda_s \bar{\mathbf{S}} \\ \lambda_t \bar{\mathbf{T}} \end{pmatrix} \bar{\mathbf{x}} \right\|_2^2. \quad (22)$$

The joint tuning of the two regularization parameters λ_s and λ_t becomes now a two-dimensional minimization and the GCV criteria can still be applied.

Some results illustrating this spatio-temporal regularization applied to the MHD model and LASCO images are presented and discussed in Section 4.2.1 and 4.3 below.

4.1.2. Co-rotating Regularization

We introduce another regularization operator, this time acting jointly in the spatial and time domain, to improve the spatio-temporal regularization. Its purpose is to prevent the concentration of the density in the vicinity of the plane of the sky (containing the Sun's center). This plane rotates in the Carrington coordinate system, as it is always orthogonal to the observer's LOS. Thus we construct an operator that filters the corona, selecting the undesirable co-rotating components, and hope that such components are prominently artifacts and not intrinsic to the corona itself. The technical detail of the construction of this regularization operator (\mathbf{C}) is presented in Appendix C.

The new minimization problem to be solved is

$$\hat{\mathbf{x}} = \underset{\bar{\mathbf{x}} \geq 0}{\operatorname{argmin}} \left(\|\mathbf{y} - \bar{\mathbf{A}}\bar{\mathbf{x}}\|_2^2 + \lambda_s^2 \|\bar{\mathbf{S}}\bar{\mathbf{x}}\|_2^2 + \lambda_t^2 \|\bar{\mathbf{T}}\bar{\mathbf{x}}\|_2^2 + \lambda_c^2 \|\mathbf{C}\bar{\mathbf{x}}\|_2^2 \right). \quad (23)$$

We now have three regularization parameters; their optimal determination is not straightforward and will be discussed when applied to a model and to LASCO images.

4.2. Application to the Dynamic Model of the Corona

4.2.1. Reconstruction with Spatial and Temporal Regularizations: Influence of the Relative Weight of the Two Regularizations

We now perform time-dependent tomography using Equation (21) and 14 synthetic pB images from the MHD model of the corona described in Appendix A. Figure 9 displays reconstructions with several choices of the temporal regularization parameter λ_t , the value of λ_s being equal to the optimum found in the case of static reconstructions ($\lambda_s = 2.2 \times 10^{-6}$).

First, looking at the bottom row of this figure corresponding to the optimal choice of the regularization parameters, we note a net improvement over all static reconstructions, even the solutions that use masking or radial weighting (see the second column of Figure 5). This solution exhibits fewer ZDA but there are not completely eradicated and we do not reach the quality of the ideal case of reconstructing a static model as shown in Figure 2. A quantitative assessment will be presented in Section 4.4.

Second, we find that the solution is highly sensitive to the temporal regularization parameter (λ_t). If λ_t is large, the time variation of the solution is annihilated and the solution has the same drawback (many ZDA) as the static inversion. On the flip side, if λ_t is low, the time variation of the solution is largely unconstrained and exhibits the same pitfalls as those crippling the time-dependent reconstruction with spatial regularization alone. The major problem in this case is a concentration of material in the plane of the sky corresponding to the unique view-point associated with each time/image and corollary, large voids in front of (and behind) the Sun as viewed from the observer.

The optimal values of the spatial and temporal regularization parameters are verified by calculating the RMS error normalized by the variance — see Equation (15) — averaged over the distance to the Sun and taking into account only 10 days out of 14 since the first and last two days are less regularized in time. The result is displayed in the top-left panel of Figure 10 and shows a sharp transition at λ_t around 3×10^{-4} . Above this threshold, the reconstruction swings to a static reconstruction regime with a large number of ZDA. The shape of the contours organized along the diagonal indicates a coupling between the two parameters which implies that the optimization is prominently controlled by the ratio of the two parameters.

The optimal settings of these regularization parameters has to be done without knowing the reconstruction error. We therefore test the two different scores described at the end of Section 2.2.1, namely the CGV and L-curve. As shown in the top-right panel of Figure 10, the GCV score fails since its minimum is only asymptotically reached for $\lambda_t = \lambda_s = 0$. This behavior is well described by Hansen (1992) in the case of correlated errors that is exactly the case here: when the temporal regularization is too weak the solution has a smaller residual but is non-physical, exhibiting concentration of material in the plane of the sky, instead of being simply randomly noisy. On the other hand, the L-curve method is able to find an optimal setting as shown in the two bottom panels of Figure 10. In the case of two regularization parameters, the L-curve becomes an “L-surface” (bottom-left panel) where the optimal setting corresponds to the maximum of the Gaussian curvature (bottom-right panel). Knowing that the L-curve has a tendency to over-regularize (Golub and Von Matt, 1997), we chose optimal values slightly smaller than those given by the L-surface maximum curvature and still along the maximum diagonal of the RMS error plot: $\lambda_s = 2.2 \times 10^{-6}$, $\lambda_t = 1.7 \times 10^{-6}$.

4.2.2. Reconstruction with the Co-rotating Regularization

We now test the time-dependent reconstruction with spatio-temporal and co-rotating regularizations as expressed by Equation (23), with various choices of the temporal and co-rotating regularization parameters, the spatial regularization being set to its previous optimal value at $\lambda_s = 2.2 \times 10^{-6}$. These results are displayed in Figures 11 and 12.

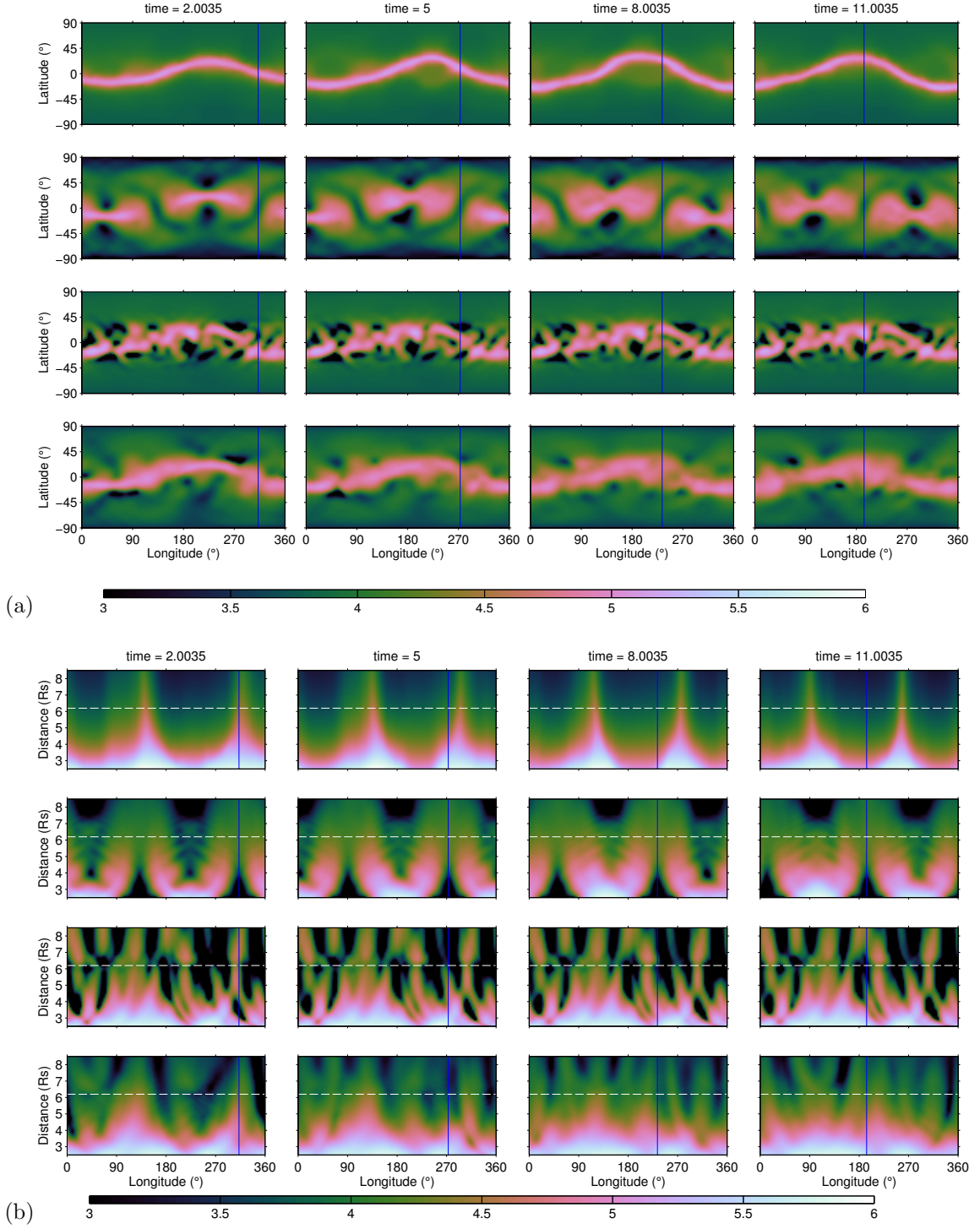


Figure 9: (a) Illustration of the spatio-temporal regularized dynamic reconstruction of a dynamic model, for 3 different settings of the regularization parameters. The 16 panels represent shells at a constant radius ($r = 4.05 R_{\odot}$) of the electron density in units of cm^{-3} using a logarithmic scale. Each column corresponds to a reconstruction of the corona at a given time. The first (top) row corresponds to the dynamic model and the next 3 rows to the different reconstructions with the temporal regularization parameter (λ_t) set to 0 (second row), 2×10^{-5} (third row), and 1.7×10^{-6} (fourth, bottom row). The value of the spatial regularization parameter is the same for the three reconstructions ($\lambda_s = 2.2 \times 10^{-6}$). The blue vertical line corresponds to the Carrington longitude of the observer. (b) Same as (a) with the panels representing the equatorial plane in polar coordinates.

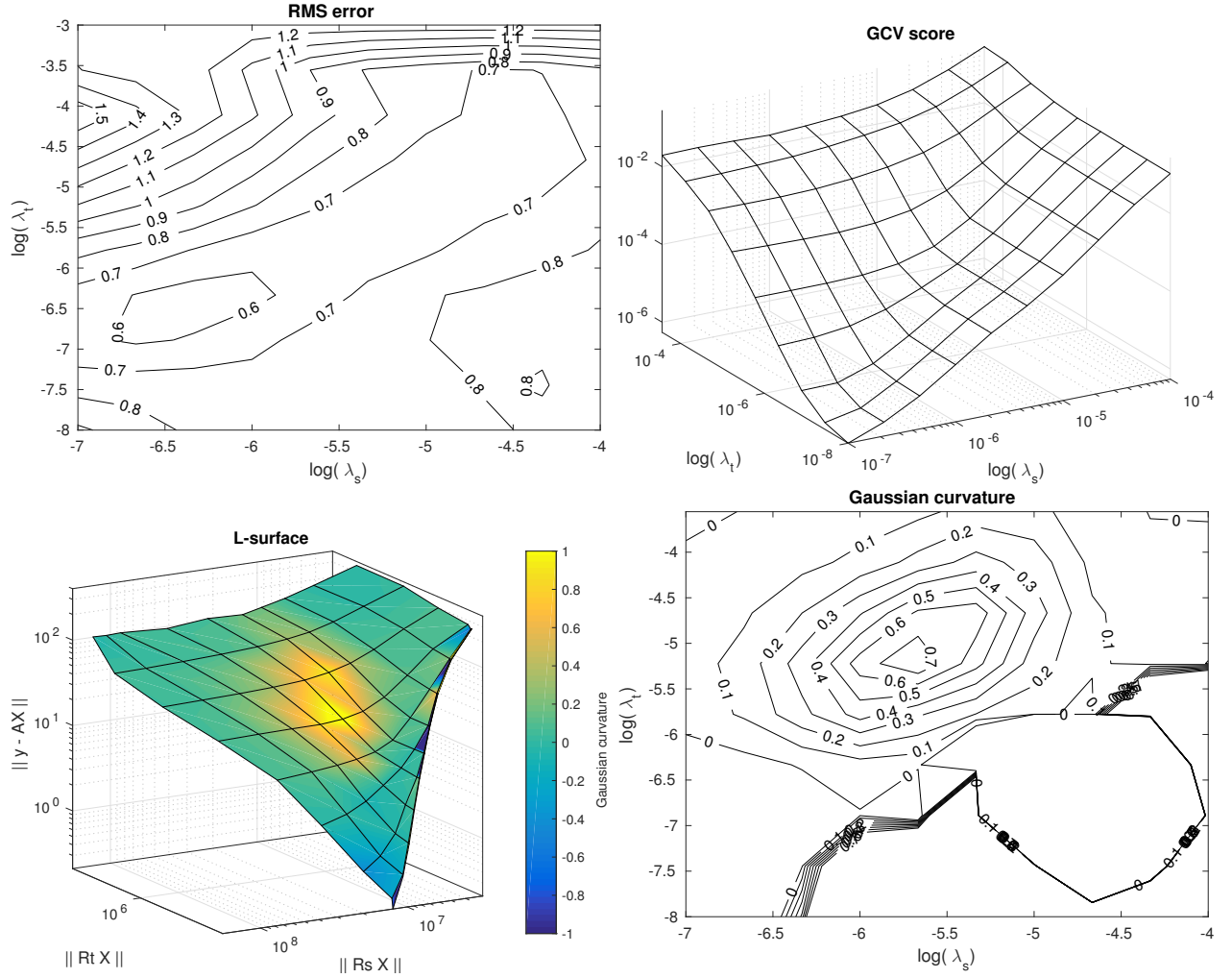


Figure 10: Illustration of the RMS reconstruction error (top-left), GCV score (top-right), L-surface (bottom-left), L-surface Gaussian curvature (bottom-right) as a function of the spatial (λ_s) and temporal (λ_t) regularization parameters.

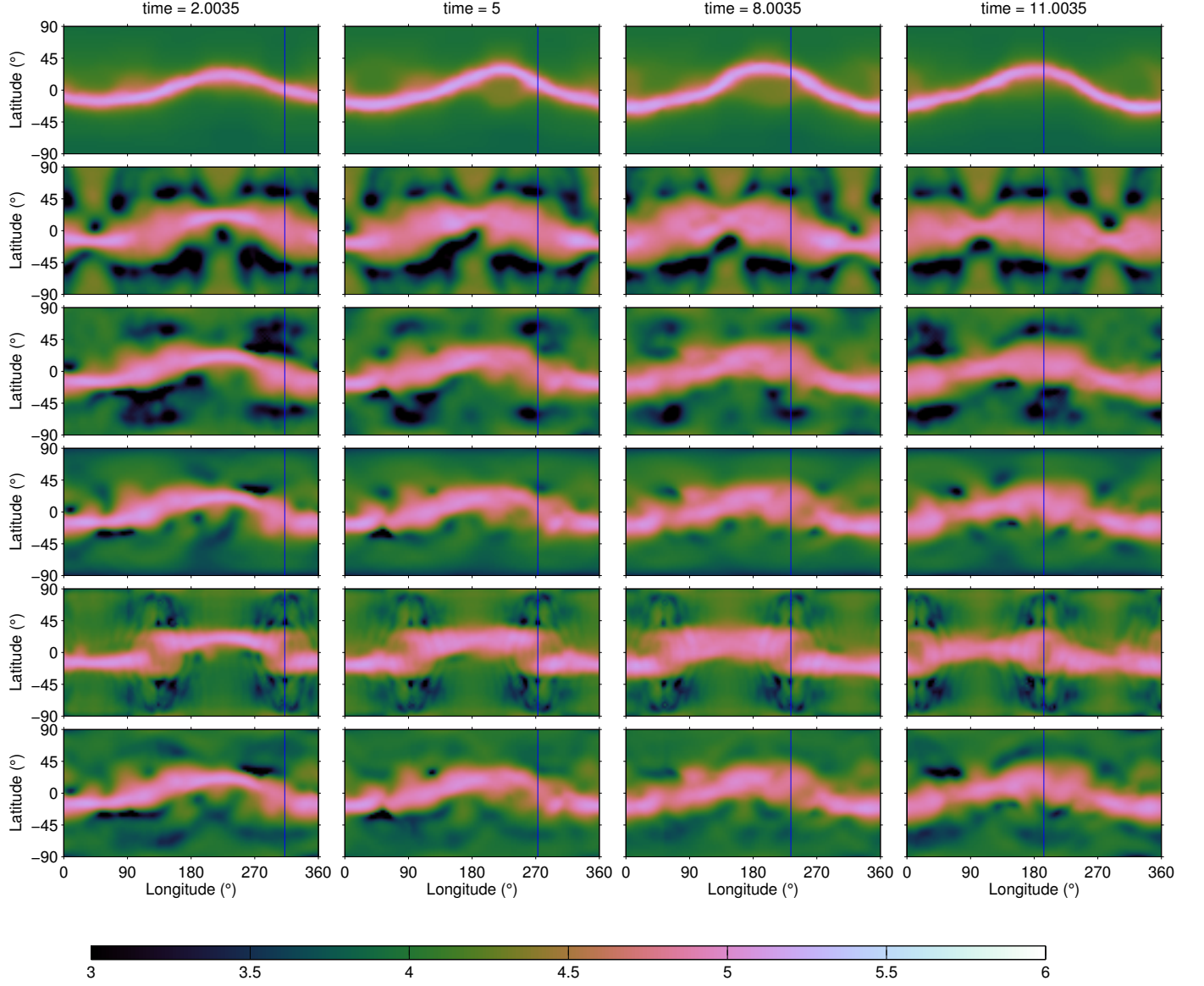


Figure 11: Illustration of dynamic reconstructions of a dynamic model using co-rotating regularization. The 24 panels represent spherical shells at $4.05 R_{\odot}$ of the electron density in units of cm^{-3} using a logarithmic scale. The first row is the dynamic model and the last 5 rows show the reconstructions with various settings of the temporal and co-rotating regularization and with the same spatial regularization ($\lambda_s = 2.2 \times 10^{-6}$). From top to bottom: no temporal regularization and co-rotating optimum regularization ($\lambda_t = 0, \lambda_c = 2 \times 10^{-7}$), small temporal regularization and co-rotating optimum regularization ($\lambda_t = 1 \times 10^{-6}, \lambda_c = 2 \times 10^{-7}$), temporal regularization optimum and small co-rotating regularization ($\lambda_t = 1.7 \times 10^{-6}, \lambda_c = 1 \times 10^{-10}$), temporal regularization optimum and large co-rotating regularization ($\lambda_t = 1.7 \times 10^{-6}, \lambda_c = 1 \times 10^{-5}$), temporal and co-rotating optimum regularizations ($\lambda_t = 1.7 \times 10^{-6}, \lambda_c = 2 \times 10^{-7}$).

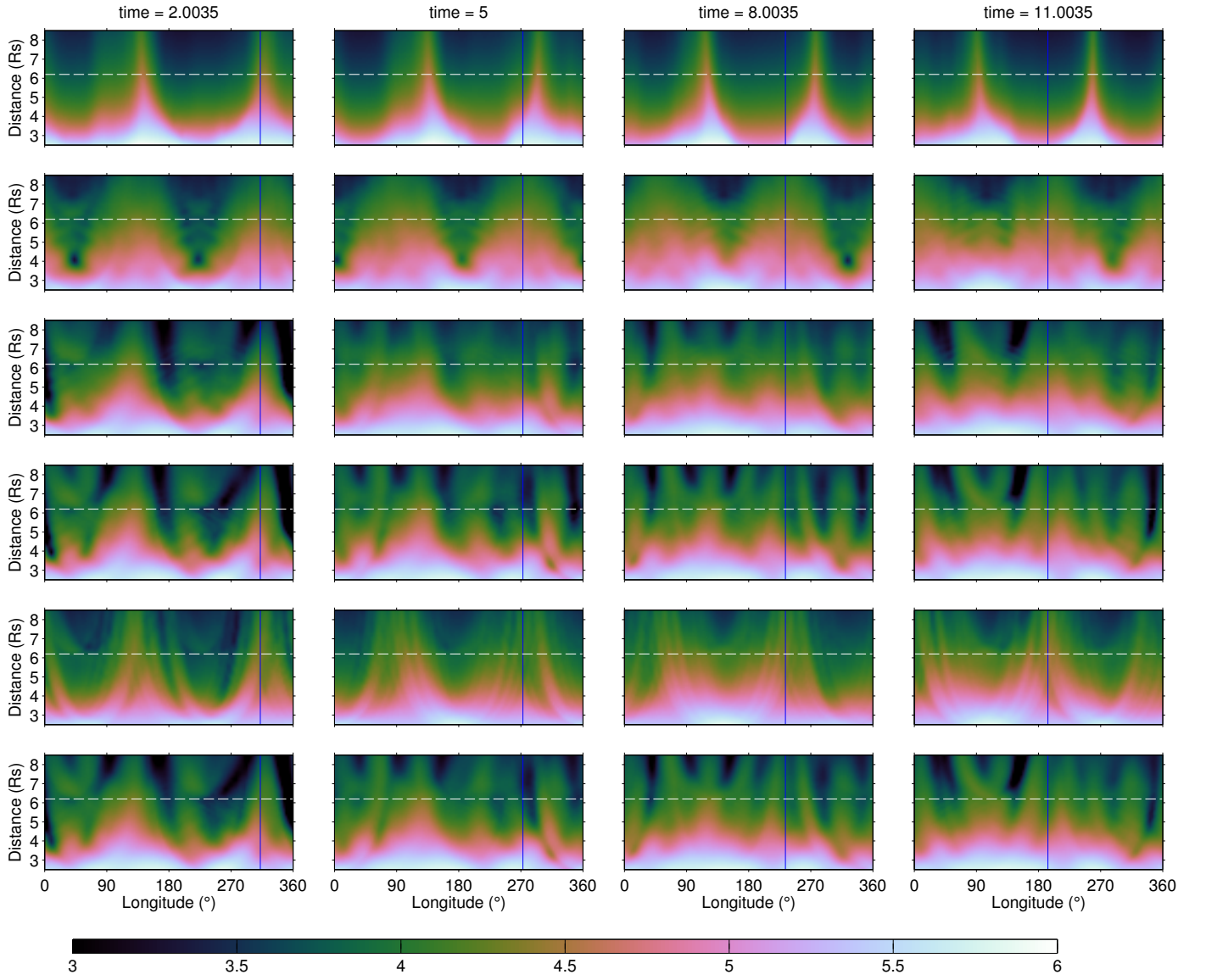


Figure 12: Same as Figure 11 with the panels representing the equatorial plane in polar coordinates.

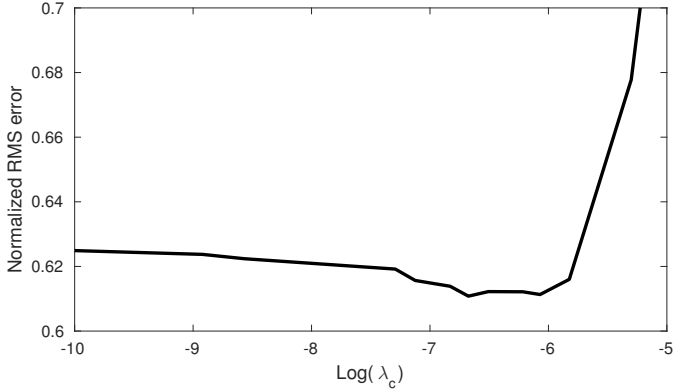


Figure 13: RMS error normalized by the standard deviation of the model, as a function of the co-rotating regularization parameter λ_c for fixed values of the spatial and temporal regularization parameters ($\lambda_s = 2.2 \times 10^{-6}$ and $\lambda_t = 1.7 \times 10^{-6}$).

We first examine whether the co-rotating regularization may simply replace the temporal regularization, allowing more freedom for the time variation and simultaneously avoiding the concentration in the plane of the sky. This case is displayed in the second row of both figures. It appears that this solution is inferior (more ZDA) to the spatio-temporal regularization presented in the previous section, see the last row of Figure 9. Even with a small amount of temporal regularization (but less than that optimally found for the spatio-temporal regularization only), the addition of the co-rotating matrix does not help, see third row. A temporal regularization at the same level as before (spatio-temporal regularization without co-rotating) is thus required. As a consequence, the introduction of the co-rotation minimization does not improve the time resolution of the solution.

The three last rows in Figures 11 and 12 display reconstructions with fixed optimal spatial and time regularization parameters (λ_s and λ_t) and three very different values of λ_c : 1×10^{-10} , 2×10^{-7} and 1×10^{-5} . This experiment shows that a large amount of co-rotating regularization (fifth row) leads to a poor solution, with perhaps less ZDA, but presenting strange features absent in the model and a poorly recovered neutral sheet.

To quantitatively assess the effect of this regularization, we plot in Figure 13 the RMS error normalized by the variance — see Equation (15) — averaged over the radial distance to the Sun, as a function of the co-rotating regularization parameter λ_c (still with λ_s and λ_t at their optimal values). Indeed, a small amount ($\approx 2 \times 10^{-7}$) of co-rotating regularization slightly improves the reconstruction. This case is displayed in the last rows of Figures 11 and 12 and can be compared with the fourth row with almost no co-rotating regularization.

Figure 13 shows again that, increasing λ_c just above its best value, rapidly degrades the solution to situations even worse than without co-rotating regularization. This can be tentatively explained by the fact that too much co-rotating

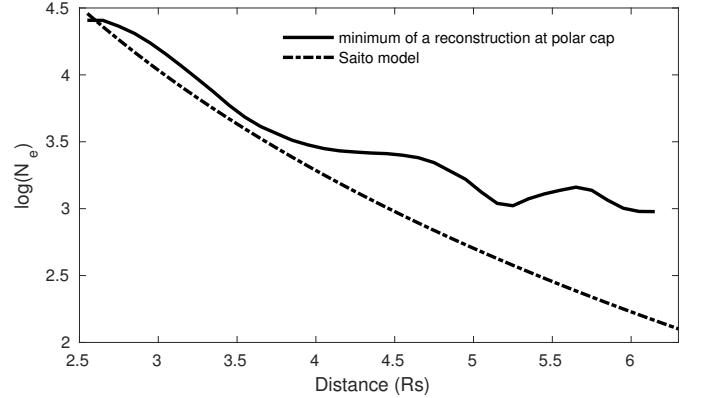


Figure 14: Radial profiles of several backgrounds representing the minimum of the coronal radiance. The solid line represents the minimum of a reconstruction in radially increasing polar caps and the dotted-dashed line represents polar profile of the axis-symmetric model of Saito et al. (1970).

regularization does remove legitimate co-rotating components present in the model, where a co-rotating component is any solution (x) that satisfies Equation (C.1); however, as explained in Appendix C, solutions that satisfy azimuthal symmetry are not penalized. As the MHD model has lower boundary conditions set by magnetograms, there are likely components of the model that are unwittingly penalized by the regularization matrix we constructed.

4.2.3. Reconstruction with a Minimal Background Prior

We now consider the possible advantage of constraining the solution to a minimal background of the electron density (N_e) as described in Section 2.2.2 using the best parameter values obtained so far, *i.e.* with co-rotating spatio-temporal regularization ($\lambda_s = 2.2 \times 10^{-6}$; $\lambda_t = 1.7 \times 10^{-6}$ and $\lambda_c = 2 \times 10^{-7}$).

We consider the axis-symmetric model of Saito et al. (1970) for the corona of the minimum type and more precisely, its polar profile to build a spherically symmetric model of the minimal background:

$$N_e(r) = \left[\frac{1.545}{r^{16}} + \frac{0.079}{r^6} \right] \times 10^8 \text{ cm}^{-3}. \quad (24)$$

Figure 14 compares this profile with that resulting from the previous regularized inversion (without the background constraint). This latter profile is obtained by taking the minima of the electron density on successive polar caps at increasing radius and limited by a small cone centered on the polar axis. One can see that the Saito profile does provide a satisfactory minimal background up to $4 R_\odot$; beyond, the reconstructed profile is affected by noise.

In order to obtain a model that is closer to the data, we can even scale the model in amplitude. The scaling coefficient which minimizes the least-square difference between the two is

$$\hat{a} = \frac{\mathbf{m}^\top \mathbf{p}}{\mathbf{m}^\top \mathbf{m}}, \quad (25)$$

where \mathbf{p} is the measured minimum N_e radial profile, \mathbf{m} the Saito model and the summation extends over the whole radial range. Using the LASCO-C2 data, we obtain a scaling coefficient of 1.14.

Figure 15 displays the results of the reconstruction that incorporates the above background. They can be compared with the last rows of Figures 11 and 12. Visually, the images are indistinguishable. Indeed, we expect the introduction of a minimal background to essentially replace the zero values in the ZDA to the minimal background values. But these patches remain much lower than their surroundings and thus appear as artifacts. However, and as it will be addressed later in the discussion, if we compare the RMS errors of reconstructions with and without the background, we do see a slight improvement.

4.3. Application to the LASCO-C2 Images

We now apply the time-dependent tomography to the set of 53 LASCO-C2 pB images described in Appendix B and display the results in Figure 16 using the three procedures (spatio-temporal regularization + co-rotating regularization + minimal background) optimally tuned on the basis of the MHD model, *i.e.* with the same values for $\lambda_s, \lambda_t, \lambda_c$.

The outcome of the tomographic reconstructions of the LASCO images is similar to that of the MHD model images. In particular, the reconstruction with the spatio-temporal regularization alone (first row) outperforms all static reconstructions (compare with Figure 7). Similarly, the addition of a co-rotating regularization is disappointing since it does not improve significantly the reconstruction (second row). Therefore, the tentative explanation given above in Section 4.2.2 of the presence of more intrinsic co-rotating components in the model than in the real corona cannot be invoked to explain the lack of benefit of the co-rotating regularization.

4.4. Discussion and comparison

Figure 17 presents a quantitative assessment of the reconstructions performed with the MHD model and LASCO images in terms of ZDA number and RMS error normalized by the standard deviation of the model in the former case and RMS residual normalized by the variance of the data in the latter case. In essence, these figures confirm the qualitative conclusions based on the displayed shells of the time-dependent reconstructions (Figures 9, 11, 12, 15, and 16). The addition of the co-rotating regularization offers only a marginal improvement in both cases, MHD model and LASCO images (same amount of ZDA but very slight decrease of the RMS error). The introduction of the background does not provide any noticeable quantitative gain on the reconstruction in both cases as best seen on the RMS error and residual curves. The number of ZDA in the two reconstructions is larger with the background but this effect is misleading. On the one hand, in the absence of background, this number is the percentage of exactly

null voxels which are strictly artifacts since the electron density cannot be exactly zero on physical grounds. On the other hand, when the background is included, we only count the voxels at the level of the background and that includes some voxels at physically acceptable density values thus overestimating the number of artifacts.

Comparing now these figures with those corresponding to the static reconstructions (Figures 6 and 8), we can appreciate the net improvement resulting from the time-dependent inversion. It reduces the number of ZDA by a factor of 30, from $\approx 3\%$ to $\approx 0.1\%$ and the RMS error by a factor ≈ 2 . Butala et al. (2010) observed a similar trend when they performed a Kalman time-dependent inversion of STEREO/COR1 data, but the improvement on their number of ZDA was only a factor 2 (from $\approx 5\%$ to $\approx 2.5\%$), which is much less than what we have achieved. However, we must keep in mind that Butala et al. (2010) reconstructed the corona between 1.5 and $3.3 R_\odot$ where one would expect more ZDA due to larger dynamical effects in the innermost corona.

5. Conclusion

In this article, we considered the main problem crippling solar rotational tomography, namely the assumption of a stable corona whereas it is intrinsically dynamic even during the minima of solar activity. Using a dynamic MHD model of the corona, we showed that a static reconstruction of the three-dimensional electron density results in severe artifacts that do not appear when applied to a static corona. We addressed the problem using two different approaches: i) mitigation of the temporal variation in the framework of a regularized static inversion, and ii) a true time-dependent inversion.

Our main results based on tests performed on synthetic images constructed from this dynamic MHD model and on real LASCO-C2 images of the corona are summarized below.

- Crucial to testing our procedure and properly tuning the regularization parameters was the introduction of a time-dependent MHD model of the corona based on observed magnetograms to build a time-series of synthetic images of the corona.
- Our mitigation procedures — multiple masking with simple juxtaposition and recursive combination of solutions, radial weighting with a mean radial intensity profile or an exponential profile — do not convincingly improve the reconstruction.
- A true time-dependent inversion with spatio-temporal regularization does improve the situation and convincingly reduces the artifacts by a factor 30 and the normalized RMS error by a factor 2.
- The introduction of an additional spatio-temporal regularization that penalizes the coronal structures

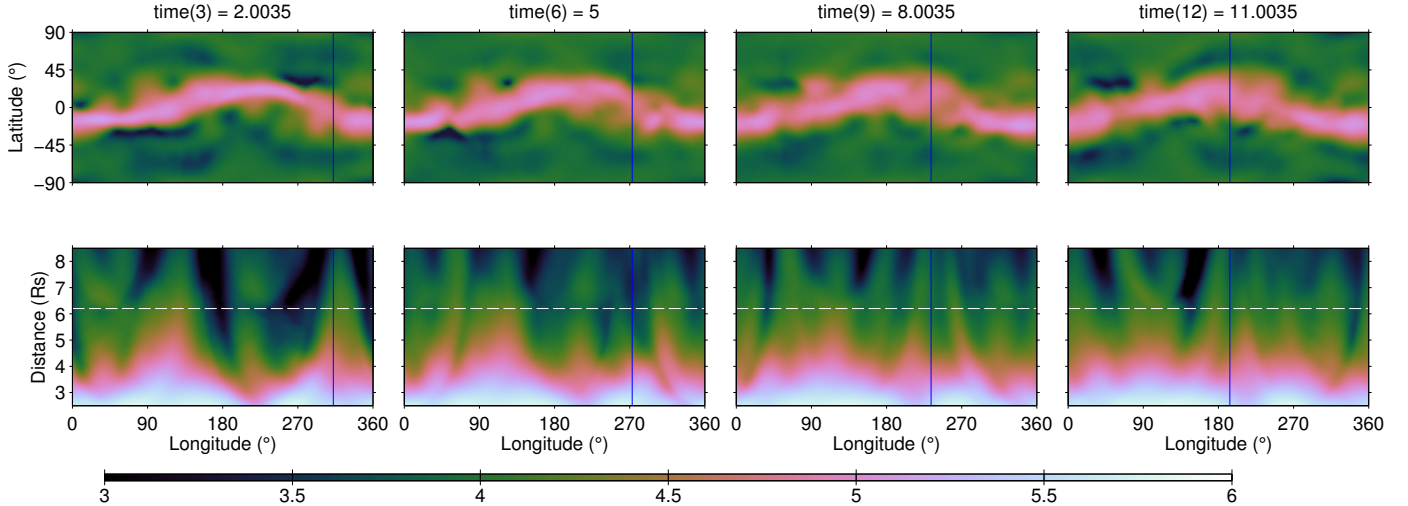


Figure 15: A dynamic reconstruction method with a background corona applied to the dynamic model. The panels represent slices of the tomographic determinations of the electron density in units of cm^{-3} using a logarithmic scale. The first row corresponds to spherical shells with radius of $4.05 R_{\odot}$ and the second row to the equatorial plane in polar coordinates.

that are apparently fixed for the observer turns out to be disappointing. However it could potentially improve the reconstruction when using more frequent images.

- Whereas non-physical densities, although greatly reduced, are still present, our dynamic reconstruction appears qualitatively superior, exhibiting a generally smoother and more connected, *i.e.* more physically reasonable, reconstructed streamer belt.

Future work will consider a possible improvement of the co-rotation regularization and will ultimately consist in applying our time-dependent SRT procedure to the whole set of LASCO-C2 images presently extending over 20 years, that is almost two solar cycles. It is hoped that the resulting four-dimensional estimates of the electron density will provide insight into the coronal and solar wind processes.

Acknowledgements

We thank B. Boclet and A. Llebaria for processing the LASCO-C2 pB images. The LASCO-C2 project at the Laboratoire d'Astrophysique de Marseille is funded by the Centre National d'Etudes Spatiales (CNES). LASCO was built by a consortium of the Naval Research Laboratory, USA, the Laboratoire d'Astrophysique de Marseille (formerly Laboratoire d'Astronomie Spatiale), France, the Max-Planck-Institut für Sonnensystemforschung (formerly Max Planck Institute für Aeronomie), Germany, and the School of Physics and Astronomy, University of Birmingham, UK. SOHO is a project of international cooperation between ESA and NASA.

Appendix A. The Time-dependent MHD Model of the Corona

In order to simulate a time-dependent solar corona, we used a time-series of steady-state MHD models. Each MHD model in the series differs only by the input magnetogram, one per day, for the time period corresponding to CR2077 (November 2008). These magnetograms were produced by the data assimilation model of Upton and Hathaway (2014), fed by HMI data. The MHD model, described by van der Holst et al. (2014), and known as the Alfvén wave solar model (AWSoM), is a global model from the upper chromosphere to the corona and the heliosphere. The coronal heating and solar wind acceleration are addressed with low-frequency Alfvén wave turbulence. The injection of Alfvén wave energy at the inner boundary is such that the Poynting flux is proportional to the magnetic field strength. The three-dimensional magnetic field topology is simulated using magnetogram data. This model does not impose open-closed magnetic field boundaries; those develop self-consistently. The physics includes the following:

1. The Alfvén waves are partially reflected by the Alfvén speed gradient and the vorticity along the field lines. The resulting counter-propagating waves are responsible for the nonlinear turbulent cascade. The balanced turbulence due to uncorrelated waves near the apex of the closed field lines and the resulting elevated temperatures are addressed.
2. The turbulent wave dissipation employs the results of the theories of linear wave damping and nonlinear stochastic heating.
3. The model incorporates collisional and collisionless heat conduction.

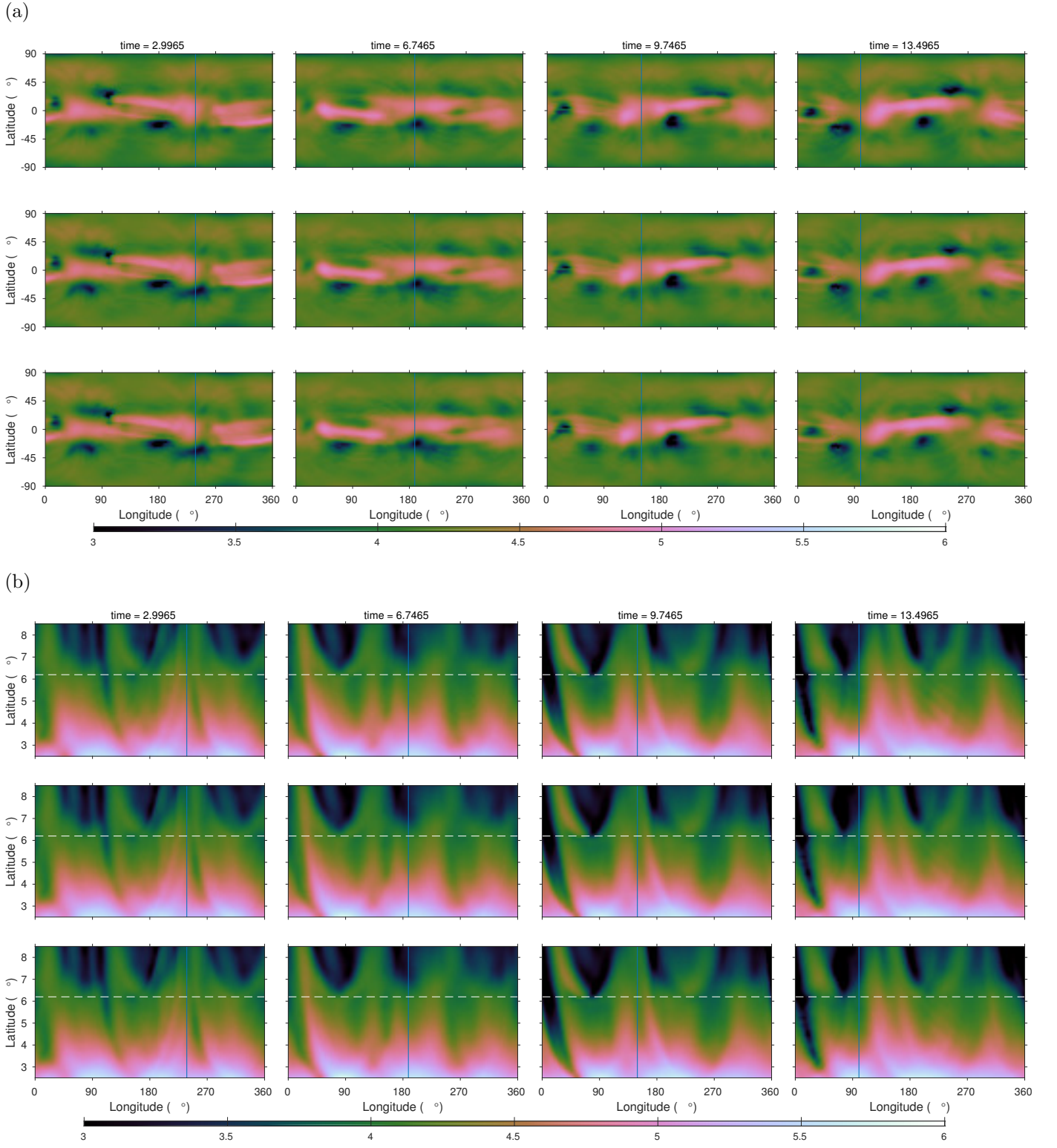


Figure 16: (a) Illustration of the spatio-temporal regularized dynamic reconstruction of LASCO-C2 images, for the three dynamic reconstruction methods. The panels represent shells at a constant radius ($r = 4.05 R_{\odot}$) of the electron density in units of cm^{-3} using a logarithmic scale. Each column corresponds to a reconstruction of the corona at a given time. The first (top) row corresponds to a reconstruction with the S and T matrices, the second row to reconstruction with the S , T and C matrices and the bottom row to a reconstruction with the S , T and C matrices and a background. The blue vertical line corresponds to the Carrington longitude of the observer. (b) Same as (a) with the panels representing the equatorial plane in polar coordinates.

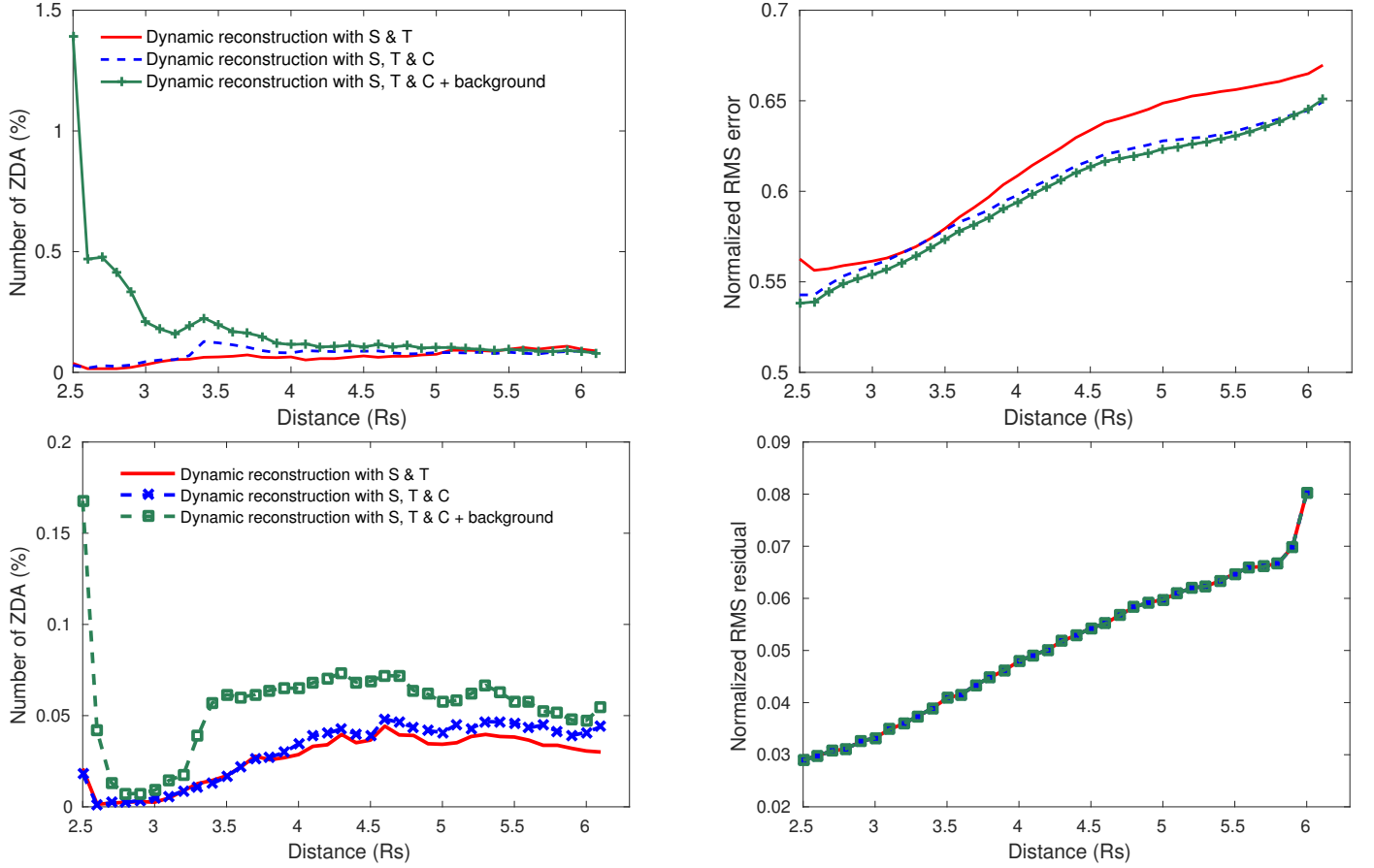


Figure 17: Quality of the solution in spherical shells of increasing distance from the Sun for the three dynamic reconstruction methods applied to 14 pB images of the dynamic MHD model (top panels) and to 53 LASCO-C2 pB images (bottom panels). The two left panels display the percentage of ZDA. The top-right panel displays the RMS error normalized by the standard deviation of the model and the bottom-right panel displays the RMS residual error normalized by the standard deviation of the image pixels. In the latter the three curves are superimposed.

Note that in the time interval between performing the simulations presented here and publication of the article of [van der Holst et al. \(2014\)](#), the AWSoM was updated to employ three different temperatures, namely the isotropic electron temperature and the parallel and perpendicular ion temperatures.

The 3D model of the electron density N_e is discretized on a spherical grid which rotates with the Sun and has bins equally spaced in latitude and longitude with a bin size of 1° and in radius extending from $2.5 R_\odot$ to $20 R_\odot$ with a bin size of $0.05 R_\odot$. It is illustrated in Figure A.18.

Synthetic images are constructed by sub-sampling the model to a resolution of 3° in latitude and longitude and $0.1 R_\odot$ radially, and integrating the Thompson scattering along each line-of-sight corresponding to each pixel. They have the same characteristics as the LASCO-C2 images taken in November 2008, same field-of-view ($2.5 R_\odot$ to $6.2 R_\odot$) and view angles.

Appendix B. The LASCO-C2 Images

The LASCO-C2 instrument routinely acquires unpolarized images of 1024^2 pixels and polarization sequences composed of three images with polarizers oriented at 60° from each other and an additional unpolarized image of the same format of 512^2 pixels. The cadence of the polarization sequences is typically one per day but has been progressively increased as more telemetry became available. In addition, high-cadence sequences have been obtained for specific purposes. Such a sequence at four images per day has been used by [Frazin et al. \(2010\)](#) for their tomographic analysis and we retained it for the present tests. The data set consists of 53 sequences, roughly evenly spaced in time, starting at about 21:00 UT on 15 March 2009 and ending at about 15:00 UT on 29 March, which falls within Carrington Rotation 2081. The procedures to correct and calibrate the LASCO-C2 images have however been substantially improved in the meantime. The most recent description of the pipeline processing of the LASCO-C2 images is given by [Lamy et al. \(2014\)](#) and it produces fully corrected and calibrated images of the polarized radiance pB and of the radiance of the K-corona B_K . It incorporates an improved absolute radiometric calibration ([Gardès et al., 2013](#)) and slight corrections of the exposure times. Additional corrections have been introduced thereafter, incidentally as a result of finding stray effects in the very first tests of our tomographic reconstruction. First an error has been detected in the orientation of the images which was corrected and even more important, the complex (because of the presence of the pylon holding the occulter) vignetting function of the coronagraph has been refined. As a consequence, the whole set of LASCO-C2 images has been reprocessed. Whereas LASCO-C2 has a field-of-view extending from $2.2 R_\odot$ to $6.2 R_\odot$, in practice the inner boundary is set to $2.5 R_\odot$ to avoid interferences from the bright diffraction fringe surrounding the occulter.

Solving the inverse problem to reconstruct the coronal density requires to build the projection matrix (\mathbf{A}), which is determined by the geometry and the physics of the problem. For each pixel located between $2.5 R_\odot$ and $6.2 R_\odot$, the geometry of the line-of-sight is specified using the information in the headers of the LASCO-C2 images and in the ancillary data, *i.e.* date of observation, attitude and location of the SOHO satellite, heliographic latitude, which is the tilt angle of the ecliptic with respect to the solar equatorial plane also called the B_0 angle. The Thomson scattering function is determined for each line-of-sight and summed over four adjacent lines-of-sight. Once we have built the matrix \mathbf{A} for the LASCO images of size 512^2 pixels, we resample the images with a factor 2 to obtain images of size 256^2 pixels to be used for the reconstruction. This summation increases the accuracy of the coefficients of the matrix.

Appendix C. Co-rotating Regularization

We first define the operator (\mathbf{R}) which rotates a static corona $x(r, \theta, \phi)$ around the polar axis by an angle (φ) via

$$\mathbf{R}(\varphi)x(r, \theta, \phi) \equiv x(r, \theta, \phi + \varphi). \quad (\text{C.1})$$

The implementation of such a rotation operator needs some interpolation scheme since the rotation angle (φ) may be a non-integer longitude shift and we chose a simple linear interpolation. We then define \mathbf{R}_i such that $\mathbf{R}_i \equiv \mathbf{R}(\varphi_i)$ where φ_i is the angle between two successive images taken at times t_i and t_{i+1} . Let \mathbf{x}_i be the solution at time t_i , then the rotating components satisfy:

$$\forall i \quad \mathbf{R}_i \mathbf{x}_i - \mathbf{x}_{i+1} = 0$$

and are therefore solution of the system $\mathbf{D}\mathbf{x} = 0$, where the linear operator \mathbf{D} is:

$$\mathbf{D} = \begin{pmatrix} \mathbf{R}_1 & -\mathbf{I} & & & \\ & \mathbf{R}_2 & -\mathbf{I} & & \\ & & \ddots & \ddots & \\ & & & \mathbf{R}_{N_t-1} & -\mathbf{I} \end{pmatrix}. \quad (\text{C.2})$$

The regularization operator is then the projection onto the null space of \mathbf{D} , since it extracts the co-rotating components of a time-dependent solution and will tend to lower them.

This rotation-differential matrix \mathbf{D} is redundant and operates only on (ϕ, t) slices at any given radius and latitude (r, θ) : $\mathbf{D} = \mathbf{D}_{\text{slice}} \otimes \mathbf{I}_{N_r \times N_\theta}$. To build a basis of the null space of \mathbf{D} , we only need to build a basis (\mathbf{L}) of the null space of $\mathbf{D}_{\text{slice}}$ ($\ker(\mathbf{D}_{\text{slice}})$). For this, we compute its singular value decomposition: $\mathbf{D}_{\text{slice}} = \mathbf{U}\mathbf{\Sigma}\mathbf{V}^\top$ and retain the last columns of \mathbf{V} corresponding to the null singular values in $\mathbf{\Sigma}$. We then need to remove from $\ker(\mathbf{D}_{\text{slice}})$ the sub-space of ϕ -invariant vectors because we do not want to penalize them in the reconstruction (there are the constant vectors in the (ϕ, t) slices space). To do so, we add

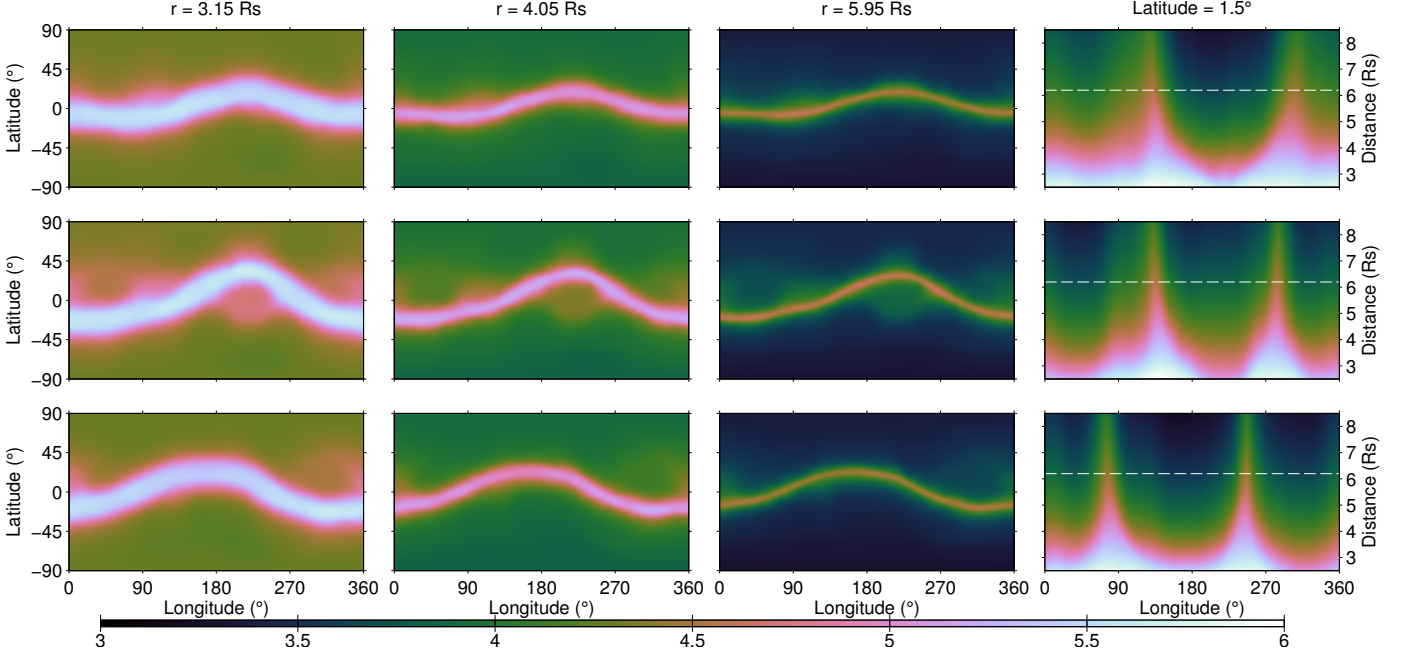


Figure A.18: Illustration of the dynamic MHD model at different dates: 21/11/2008 (first row), 27/11/2008 (second row), 04/12/2008 (third row). The 12 panels represent slices of the electron density in units of cm^{-3} using a logarithmic scale. The 3 leftmost columns correspond to spherical shells with radii of $3.15 R_{\odot}$, $4.05 R_{\odot}$ and $5.95 R_{\odot}$ and the rightmost column to the equatorial plane in polar coordinates.

a constant column vector in front of the basis \mathbf{L} , orthogonalize it and remove the unchanged first constant column vector. Retaining the same notation (\mathbf{L}) for this new basis, the desired regularization operator (\mathbf{C}) is the projection on the sub-space spanned by \mathbf{L} :

$$\mathbf{C} = \mathbf{L}\mathbf{L}^{\top} \otimes \mathbf{I}_{N_r \times N_{\theta}}. \quad (\text{C.3})$$

In the latter formulation, the co-rotating penalization is computed for each couple of latitude and radius (r, θ) and the L2 norm of the total is minimized. We find preferable to first sum the candidate solution (\mathbf{x}) along θ and then apply the co-rotating penalization to a (ϕ, t) slice summed over θ for each radius r :

$$\mathbf{C}_{\Sigma\theta} = [\mathbf{L}\mathbf{L}^{\top}(\mathbf{I}_{N_{\phi} \times N_t} \otimes \mathbf{1}_{N_{\theta}}^{\top})] \otimes \mathbf{I}_{N_r}. \quad (\text{C.4})$$

In order to further improve this regularization, it is possible to reduce the null-space of \mathbf{D} which is quite large. In particular, the above operator penalizes all components that synchronously rotates with the observer and we could try to select a more specific fraction of them. We experimented in this direction using Fourier filtering along the ϕ coordinate and extracting only the low longitudinal frequency modes which rotate synchronously, for instance taking only the even modes (or a fraction of them) corresponding to the components having a 180° longitudinal periodicity plus some of its harmonics. This did not make much difference when applied to the MHD model. Instead of operating in the Fourier space, it may be simpler trying to penalize the components that shift from being concen-

trated in plane i to plane $i + 1$ for all i , with a weighting function decreasing with the angular distance to this plane.

References

References

- Allen, D.M., 1974. The Relationship Between Variable Selection and Data Augmentation and a Method for Prediction. *Technometrics* 16, 125–127. doi:[10.1080/00401706.1974.10489157](https://doi.org/10.1080/00401706.1974.10489157).
- Barbey, N., Auchère, F., Rodet, T., Vial, J.C., 2008. A Time-Evolving 3D Method Dedicated to the Reconstruction of Solar Plumes and Results Using Extreme Ultraviolet Data. *Solar Phys.* 248, 409–423. doi:[10.1007/s11207-008-9151-6](https://doi.org/10.1007/s11207-008-9151-6), [arXiv:0802.0113](https://arxiv.org/abs/0802.0113).
- Barbey, N., Guennou, C., Auchère, F., 2013. TomograPy: A Fast, Instrument-Independent, Solar Tomography Software. *Solar Phys.* 283, 227–245. doi:[10.1007/s11207-011-9792-8](https://doi.org/10.1007/s11207-011-9792-8).
- Bro, R., De Jong, S., 1997. A fast non-negativity-constrained least squares algorithm. *Journal of chemometrics* 11, 393–401. doi:[10.1002/\(SICI\)1099-128X\(199709/10\)11:5<393::AID-CEM483>3.0.CO;2-L](https://doi.org/10.1002/(SICI)1099-128X(199709/10)11:5<393::AID-CEM483>3.0.CO;2-L).
- Butala, M.D., Hewett, R.J., Frazin, R.A., Kamalabadi, F., 2010. Dynamic Three-Dimensional Tomography of the Solar Corona. *Solar Phys.* 262, 495–509. doi:[10.1007/s11207-010-9536-1](https://doi.org/10.1007/s11207-010-9536-1).
- Byrd, R.H., Lu, P., Nocedal, J., Zhu, C., 1995. A limited memory algorithm for bound constrained optimization. *SIAM Journal on Scientific Computing* 16, 1190–1208. doi:[10.1137/0916069](https://doi.org/10.1137/0916069).
- Floyd, O., Lamy, P., Llebaria, A., 2014. The Interaction Between Coronal Mass Ejections and Streamers: A Statistical View over 15 Years (1996–2010). *Solar Phys.* 289, 1313–1339. doi:[10.1007/s11207-013-0379-4](https://doi.org/10.1007/s11207-013-0379-4).
- Frazin, R.A., 2000. Tomography of the Solar Corona. I. A Robust, Regularized, Positive Estimation Method. *Astrophys. J.* 530, 1026–1035. doi:[10.1086/308412](https://doi.org/10.1086/308412).

- Frazin, R.A., Butala, M.D., Kemball, A., Kamalabadi, F., 2005. Time-dependent reconstruction of nonstationary objects with tomographic or interferometric measurements. *The Astrophysical Journal Letters* 635, L197. doi:[10.1086/499431](https://doi.org/10.1086/499431).
- Frazin, R.A., Janzen, P., 2002. Tomography of the Solar Corona. II. Robust, Regularized, Positive Estimation of the Three-dimensional Electron Density Distribution from LASCO-C2 Polarized White-Light Images. *Astrophys. J.* 570, 408–422. doi:[10.1086/339572](https://doi.org/10.1086/339572).
- Frazin, R.A., Kamalabadi, F., 2005. Rotational Tomography For 3d Reconstruction Of The White-Light And Euv Corona In The Post-Soho Era. *Solar Phys.* 228, 219–237. doi:[10.1007/s11207-005-2764-0](https://doi.org/10.1007/s11207-005-2764-0).
- Frazin, R.A., Lamy, P., Llebaria, A., Vázquez, A.M., 2010. Three-Dimensional Electron Density from Tomographic Analysis of LASCO-C2 Images of the K-Corona Total Brightness. *Solar Phys.* 265, 19–30. doi:[10.1007/s11207-010-9557-9](https://doi.org/10.1007/s11207-010-9557-9).
- Frazin, R.A., Vázquez, A.M., Kamalabadi, F., 2009. Quantitative, Three-dimensional Analysis of the Global Corona with Multi-spacecraft Differential Emission Measure Tomography. *Astrophys. J.* 701, 547–560. doi:[10.1088/0004-637X/701/1/547](https://doi.org/10.1088/0004-637X/701/1/547).
- Frazin, R.A., Vázquez, A.M., Kamalabadi, F., Park, H., 2007. Three-dimensional Tomographic Analysis of a High-Cadence LASCO-C2 Polarized Brightness Sequence. *Astrophys. J. Lett.* 671, L201–L204. doi:[10.1086/525017](https://doi.org/10.1086/525017).
- Frazin, R.A., Vázquez, A.M., Thompson, W.T., Hewett, R.J., Lamy, P., Llebaria, A., Vourlidis, A., Burkepile, J., 2012. Intercomparison of the LASCO-C2, SECCHI-COR1, SECCHI-COR2, and Mk4 Coronagraphs. *Solar Phys.* 280, 273–293. doi:[10.1007/s11207-012-0028-3](https://doi.org/10.1007/s11207-012-0028-3).
- Gardès, B., Lamy, P., Llebaria, A., 2013. Photometric Calibration of the LASCO-C2 Coronagraph over 14 Years (1996–2009). *Solar Phys.* 283, 667–690. doi:[10.1007/s11207-013-0240-9](https://doi.org/10.1007/s11207-013-0240-9).
- Golub, G.H., Heath, M., Wahba, G., 1979. Generalized cross-validation as a method for choosing a good ridge parameter. *Technometrics* 21, 215–223. doi:[10.2307/1268518](https://doi.org/10.2307/1268518).
- Golub, G.H., Von Matt, U., 1997. Tikhonov regularization for large scale problems, in: *Workshop on Scientific Computing*, pp. 3–26.
- Hansen, P.C., 1992. Analysis of Discrete Ill-Posed Problems by Means of the L-Curve. *SIAM Review* 34, 561–580. doi:[10.1137/1034115](https://doi.org/10.1137/1034115).
- Hansen, P.C., OLeary, D.P., 1993. The Use of the L-Curve in the Regularization of Discrete Ill-Posed Problems. *SIAM Journal on Scientific Computing* 14, 1487–1503. doi:[10.1137/0914086](https://doi.org/10.1137/0914086).
- van der Holst, B., Sokolov, I.V., Meng, X., Jin, M., Manchester, IV, W.B., Tóth, G., Gombosi, T.I., 2014. Alfvén wave solar model (awsom): coronal heating. *The Astrophysical Journal* 782, 81. doi:[10.1088/0004-637X/782/2/81](https://doi.org/10.1088/0004-637X/782/2/81).
- Huang, Z., Frazin, R.A., Landi, E., Manchester, W.B., Vázquez, A.M., Gombosi, T.I., 2012. Newly Discovered Global Temperature Structures in the Quiet Sun at Solar Minimum. *Astrophys. J.* 755, 86. doi:[10.1088/0004-637X/755/2/86](https://doi.org/10.1088/0004-637X/755/2/86), [arXiv:1207.6661](https://arxiv.org/abs/1207.6661).
- Kramar, M., Airapetian, V., Mikić, Z., Davila, J., 2014. 3D Coronal Density Reconstruction and Retrieving the Magnetic Field Structure during Solar Minimum. *Solar Physics* 289, 2927–2944. doi:[10.1007/s11207-014-0525-7](https://doi.org/10.1007/s11207-014-0525-7), [arXiv:1405.0951](https://arxiv.org/abs/1405.0951).
- Kramar, M., Jones, S., Davila, J., Inhester, B., Mierla, M., 2009. On the Tomographic Reconstruction of the 3D Electron Density for the Solar Corona from STEREO COR1 Data. *Solar Phys.* 259, 109–121. doi:[10.1007/s11207-009-9401-2](https://doi.org/10.1007/s11207-009-9401-2).
- Lamy, P., Barlyaeva, T., Llebaria, A., Floyd, O., 2014. Comparing the solar minima of cycles 22/23 and 23/24: The view from LASCO white light coronal images. *Journal of Geophysical Research: Space Physics* 119, 47–58. doi:[10.1002/2013JA019468](https://doi.org/10.1002/2013JA019468).
- Lawson, C.L., Hanson, R.J., 1995. 23. Linear Least Squares with Linear Inequality Constraints. chapter 23. pp. 158–173. doi:[10.1137/1.9781611971217.ch23](https://doi.org/10.1137/1.9781611971217.ch23).
- Louis, A.K., Natterer, F., 1983. Mathematical problems of computerized tomography. *Proceedings of the IEEE* 71, 379–389. doi:[10.1109/PROC.1983.12596](https://doi.org/10.1109/PROC.1983.12596).
- Morales, J.L., Nocedal, J., 2011. Remark on algorithm 778: LBFGS-B: Fortran subroutines for large-scale bound constrained optimization. *ACM Transactions on Mathematical Software* 38, 1–4. doi:[10.1145/2049662.2049669](https://doi.org/10.1145/2049662.2049669).
- Nuevo, F.A., Huang, Z., Frazin, R., Manchester, IV, W.B., Jin, M., Vázquez, A.M., 2013. Evolution of the Global Temperature Structure of the Solar Corona during the Minimum between Solar Cycles 23 and 24. *Astrophys. J.* 773, 9. doi:[10.1088/0004-637X/773/1/9](https://doi.org/10.1088/0004-637X/773/1/9).
- Orieux, F., Giovannelli, J.F., Rodet, T., Abergel, A., 2013. Estimating hyperparameters and instrument parameters in regularized inversion Illustration for Herschel /SPIRE map making. *Astronomy & Astrophysics* 549, A83. doi:[10.1051/0004-6361/201219950](https://doi.org/10.1051/0004-6361/201219950).
- Paige, C.C., Saunders, M.a., 1982. LSQR: An Algorithm for Sparse Linear Equations and Sparse Least Squares. *ACM Transactions on Mathematical Software* 8, 43–71. doi:[10.1145/355984.355989](https://doi.org/10.1145/355984.355989).
- Saito, K., Makita, M., Nishii, K., Hata, S., 1970. A non-spherical axisymmetric model of the solar K corona of the minimum type. *Annals of the Tokyo Astronomical Observatory* 12, 53–120.
- Stark, P.B., Parker, R.L., 1995. Bounded-variable least-squares: an algorithm and applications. *Computational Statistics* 10, 129–129.
- Stone, M., 1974. Cross-Validatory Choice and Assessment of Statistical Predictions. *Journal of the Royal Statistical Society. Series B (Methodological)* 36, 111–147.
- Upton, L., Hathaway, D.H., 2014. Predicting the sun’s polar magnetic fields with a surface flux transport model. *The Astrophysical Journal* 780, 5. doi:[10.1088/0004-637X/780/1/5](https://doi.org/10.1088/0004-637X/780/1/5).
- van de Hulst, H.C., 1950. The electron density of the solar corona. *Bull. Astron. Inst. Neth.* 11, 135.
- Vázquez, A.M., Frazin, R.A., Kamalabadi, F., 2009. 3D Temperatures and Densities of the Solar Corona via Multi-Spacecraft EUV Tomography: Analysis of Prominence Cavities. *Solar Phys.* 256, 73–85. doi:[10.1007/s11207-009-9321-1](https://doi.org/10.1007/s11207-009-9321-1).
- Vázquez, A.M., Frazin, R.A., Manchester, IV, W.B., 2010. The Solar Minimum Corona from Differential Emission Measure Tomography. *Astrophys. J.* 715, 1352–1365. doi:[10.1088/0004-637X/715/2/1352](https://doi.org/10.1088/0004-637X/715/2/1352), [arXiv:1012.5953](https://arxiv.org/abs/1012.5953).
- Vázquez, A.M., Huang, Z., Manchester, W.B., Frazin, R.A., 2011. The WHI Corona from Differential Emission Measure Tomography. *Solar Phys.* 274, 259–284. doi:[10.1007/s11207-010-9706-1](https://doi.org/10.1007/s11207-010-9706-1).
- Zhang, Y., Ghodrati, A., Brooks, D., 2005. An analytical comparison of three spatio-temporal regularization methods for dynamic linear inverse problems in a common statistical framework. *Inverse Probl.* 21, 357–382. doi:[10.1088/0266-5611/21/1/022](https://doi.org/10.1088/0266-5611/21/1/022).